

UC Berkeley

UC Berkeley Previously Published Works

Title

Water Enables Efficient CO₂ Capture from Natural Gas Flue Emissions in an Oxidation-Resistant Diamine-Appended Metal-Organic Framework.

Permalink

<https://escholarship.org/uc/item/08n6p340>

Journal

Journal of the American Chemical Society, 141(33)

ISSN

0002-7863

Authors

Siegelman, Rebecca L
Milner, Phillip J
Forse, Alexander C
[et al.](#)

Publication Date

2019-08-01

DOI

10.1021/jacs.9b05567

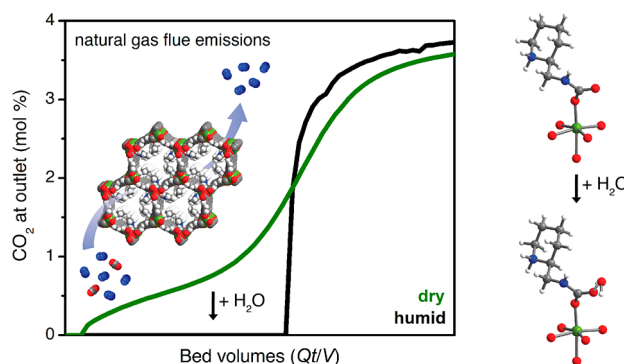
Peer reviewed

Water Enables Efficient CO₂ Capture from Natural Gas Flue Emissions in an Oxidation-Resistant Diamine-Appended Metal–Organic Framework

Rebecca L. Siegelman,^{†,‡,¶,¶} Phillip J. Milner,^{†,‡,¶,¶} Alexander C. Forse,^{†,‡,§,¶} Jung-Hoon Lee,^{||,¶} Kristen A. Colwell,[§] Jeffrey B. Neaton,^{||,¶,▽} Jeffrey A. Reimer,^{§,‡,¶} Simon C. Weston,^{○,¶} and Jeffrey R. Long^{*,†,§,‡,¶}

[†]Department of Chemistry, [‡]Berkeley Energy and Climate Institute, [§]Department of Chemical and Biomolecular Engineering, and ^{||}Department of Physics, University of California, Berkeley, California 94720, United States
[¶]Materials Sciences Division and [¶]Molecular Foundry, Lawrence Berkeley National Laboratory, Berkeley, California 94720, United States
[▽]Kavli Energy Nanosciences Institute at Berkeley, Berkeley, California 94720, United States
[○]Corporate Strategic Research, ExxonMobil Research and Engineering Company, Annandale, New Jersey 08801, United States

ABSTRACT: Supported by increasingly available reserves, natural gas is achieving greater adoption as a cleaner-burning alternative to coal in the power sector. As a result, carbon capture and sequestration from natural gas-fired power plants is an attractive strategy to mitigate global anthropogenic CO₂ emissions. However, the separation of CO₂ from other components in the flue streams of gas-fired power plants is particularly challenging due to the low CO₂ partial pressure (~40 mbar), which necessitates that candidate separation materials bind CO₂ strongly at low partial pressures (≤4 mbar) to capture ≥90% of the emitted CO₂. High partial pressures of O₂ (120 mbar) and water (80 mbar) in these flue streams have also presented significant barriers to the deployment of new technologies for CO₂ capture from gas-fired power plants. Here, we demonstrate that functionalization of the metal–organic framework Mg₂(dobpdc) (dobpdc^{4−} = 4,4′-dioxidobiphenyl-3,3′-dicarboxylate) with the cyclic diamine 2-(aminomethyl)piperidine (2-ampd) produces an adsorbent that is capable of ≥90% CO₂ capture from a humid natural gas flue emission stream, as confirmed by breakthrough measurements. This material captures CO₂ by a cooperative mechanism that enables access to a large CO₂ cycling capacity with a small temperature swing (2.4 mmol CO₂/g with ΔT ≥ 100 °C). Significantly, multicomponent adsorption experiments, infrared spectroscopy, magic angle spinning solid-state NMR spectroscopy, and van der Waals-corrected density functional theory studies suggest that water enhances CO₂ capture in 2-ampd–Mg₂(dobpdc) through hydrogen-bonding interactions with the carbamate groups of the ammonium carbamate chains formed upon CO₂ adsorption, thereby increasing the thermodynamic driving force for CO₂ binding. In light of the exceptional thermal and oxidative stability of 2-ampd–Mg₂(dobpdc), its high CO₂ adsorption capacity, and its high CO₂ capture rate from a simulated natural gas flue emission stream, this material is one of the most promising adsorbents to date for this important separation.



INTRODUCTION

The combustion of fossil fuels in the energy sector is currently responsible for the release of 32 Gt/year of CO₂ into the atmosphere, or approximately 65% of annual anthropogenic greenhouse gas emissions.^{1,2} To limit the contribution of these emissions to global climate change, mitigation strategies are needed during the transition to cleaner fuel sources.² One of the most widely studied emission mitigation strategies is postcombustion carbon capture and sequestration (CCS), in which CO₂ is selectively removed from the flue gas streams of

fossil fuel- or biomass-fired power plants and sequestered underground.^{1–4} To date, the large majority of efforts toward implementing CCS have focused on coal-fired power plants, which are currently responsible for approximately 45% of energy-related CO₂ emissions.^{4,5} However, global consumption of natural gas has been increasing steadily, and its contribution to global primary energy is anticipated to overtake

that of coal by 2040 (New Policy Scenario, International Energy Agency).⁶ Furthermore, in economies where natural gas is prevalent, such as that of the United States, the rapid transition away from coal has resulted in CO₂ emissions from the combustion of natural gas already exceeding those from coal, despite the fact that natural gas emits approximately half as much CO₂ as coal per unit electricity produced.⁷ Therefore, new materials are urgently needed for the selective removal of CO₂ from the emissions of natural gas-fired power plants.^{8–10}

The flue gas stream produced at a natural gas combined cycle (NGCC) power plant consists of approximately 74.4% N₂, 12.4% O₂, 8.4% H₂O, 3.9% CO₂, and 0.9% Ar.¹¹ Importantly, emissions from NGCC plants contain fewer pollutants than emission streams from coal-fired plants, which release SO_x, NO_x, heavy metals, and particulate matter.¹¹ These contaminants pose environmental hazards and serve as significant barriers to the deployment of CCS systems in coal-fired plants, particularly due to the known poisoning of a number of CO₂ capture materials by SO_x and NO_x.^{12–19} The CO₂ partial pressure of NGCC flue gas (~40 mbar) is also significantly lower than that of coal flue gas (~150 mbar).¹¹ As a result, gas-fired plants are cleaner-burning than coal-fired plants, but CO₂ capture from the emissions of these power stations is more technically challenging. Specifically, the U.S. Department of Energy (DoE) has set a target of 90% capture of CO₂ from the emission stream,¹¹ requiring that candidate CO₂ capture materials bind CO₂ at concentrations as low as 0.4%. Materials that meet this requirement often possess high CO₂ adsorption enthalpies,²⁰ necessitating energy-intensive cycling conditions and generating a potential trade-off between heat management and CO₂ cycling capacity.²¹

Owing to decades of development, aqueous amine solutions are the most technology-ready systems for large-scale CO₂ capture applications.^{22,23} However, amine solutions face technological barriers to deployment for CO₂ capture from NGCC power plants due to their high regeneration energy costs and susceptibility to oxidative and thermal degradation.^{24–27} As an alternative, solid adsorbents, such as zeolites, amine-functionalized silicas, porous organic networks, and metal–organic frameworks, may offer enhanced stability, greater CO₂ cycling capacities, and inherently lower regeneration energies.^{4,28–40} Despite the flourishing research areas of adsorptive CO₂ capture from coal flue gas and air, only a handful of reports have yet explored adsorbent design specifically for CCS from gas-fired power plants.^{36,41–48} More research is also needed to design adsorbents with high thermal and oxidative stabilities that can capture CO₂ selectively under humid conditions.

Recently, we^{49–53} and others^{45,54–58} have demonstrated the potential of diamine-appended variants of the metal–organic framework Mg₂(dobpdc) (dobpdc^{4−} = 4,4′-dioxidobiphenyl-3,3′-dicarboxylate) as transformative materials for carbon capture applications.⁵⁹ The unique step-shaped adsorption profiles of these frameworks enable cycling of the full CO₂ adsorption capacity with minimal temperature swings. We have further shown that the adsorption step of these materials can be tuned postsynthetically by changing the appended diamine,⁵¹ a strategy that we employed to optimize an adsorbent for CO₂ capture from coal flue gas.⁵² Our previous work posited that *primary*, *secondary* (1°/2°) diamine-appended variants of Mg₂(dobpdc) are likely the most promising for CO₂ capture from NGCC flue gas, on the basis of their low CO₂ adsorption step pressures (<1 mbar at

40 °C) and minimal hysteresis upon CO₂ desorption.⁵¹ However, these materials possess a trade-off between thermal stability and CO₂ adsorption capacity. Specifically, the largest 1°/2° diamines were the most resistant to amine volatilization during temperature-swing cycling but also underwent a steric rearrangement at half saturation (0.5 CO₂ per diamine), which led to double-stepped CO₂ adsorption profiles.⁵³ As a result, at the low partial pressures relevant for NGCC CCS systems, only the capacity of the first CO₂ adsorption step (half of the theoretical capacity) would be accessible with such materials. While two similar base frameworks were shown to resolve the issue of steric crowding to enable single-step adsorption profiles with large diamines,⁵³ the initially studied Mg₂(dobpdc)(diamine)₂ variants remain preferable due to their inexpensive components and favorable gravimetric (~3.5–4.0 mmol/g) and volumetric (~79–84 v/v) CO₂ adsorption capacities.⁵¹ Additionally, Mg₂(dobpdc) has already been prepared at the multikilogram scale,⁶⁰ facilitating rapid technology development.

Herein, we demonstrate that appending the cyclic 1°/2° diamine 2-(aminomethyl)piperidine (2-ampd) to the metal sites in Mg₂(dobpdc) alters the steric interactions and thermodynamics of CO₂ adsorption, giving rise to a material with two closely spaced adsorption steps. The adsorbent 2-ampd–Mg₂(dobpdc) (Figure 1) is thermally stable and exhibits two CO₂ adsorption steps at pressures low enough to access the full chemisorptive capacity of the material (1 CO₂ per diamine) from NGCC flue gas. Importantly, we find that

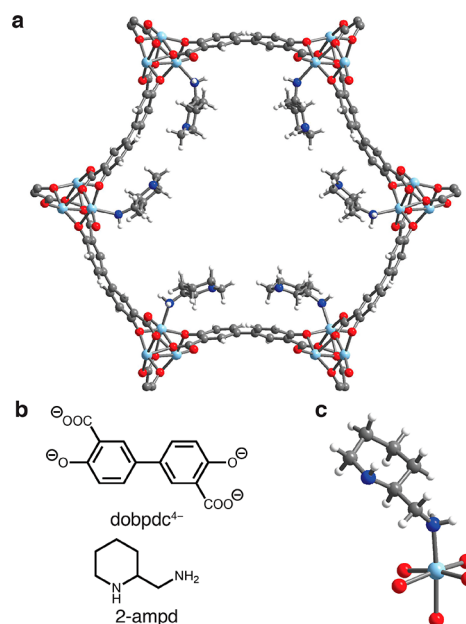


Figure 1. (a) Single-crystal X-ray diffraction structure of toluene-solvated 2-ampd–Zn₂(dobpdc), which is isostructural to 2-ampd–Mg₂(dobpdc). The left-handed diamine is depicted in the right-handed framework (space group *P*3₁21). The structure was refined with a racemic mixture of 2-ampd in an inversion-twinned crystal. The enantiomeric diamine and toluene solvent molecules are omitted for clarity. (b) Chemical structures of the ligand dobpdc^{4−} and the diamine 2-ampd. (c) First coordination sphere of the Zn(II) site depicting coordination of the left-handed enantiomer of 2-ampd. The diamines were found to coordinate exclusively through the primary amine. Light blue, blue, red, gray, and white spheres represent Zn, N, O, C, and H atoms, respectively.

the presence of water greatly improves the CO₂ adsorption characteristics of this material, enabling it to achieve ≥90% removal of CO₂ from simulated NGCC flue gas in breakthrough measurements. While other amine-functionalized adsorbents have shown improvements in CO₂ capture performance due to a humidity-induced mechanistic shift, our van der Waals (vdW)-corrected density functional theory (DFT) calculations and spectroscopy measurements show that the improved performance of 2-ampd-Mg₂(dobpdc) under humid conditions can instead be attributed to preferential stabilization of the ammonium carbamate chains formed upon CO₂ insertion. Our results demonstrate that 2-ampd-Mg₂(dobpdc) is among the most promising adsorbents identified to date for this underexplored but extremely important separation.

EXPERIMENTAL SECTION

General Procedures. ¹H NMR spectra were collected on a Bruker AMX 300 MHz spectrometer and referenced to residual dimethyl sulfoxide (δ = 2.50 ppm). Powder X-ray diffraction (PXRD) patterns were collected with a laboratory Bruker AXS D8 Advance diffractometer with Cu K α radiation (λ = 1.5418 Å) or at the Advanced Photon Source with synchrotron radiation (λ = 0.45399 Å), as specified in the figure captions. Additional details for synchrotron PXRD experiments under controlled atmospheres are given in Supporting Information (SI) Section S15. All synthetic manipulations were carried out under air unless noted otherwise. All solvents and reagents, including diamines, were purchased from commercial sources and used without further purification unless otherwise noted. The linker H₄ dobpdc was purchased from Hangzhou Trylead Chemical Technology Co. The linker H₄ dotpdc was prepared according to the literature procedure.⁵³ The metal-organic frameworks Mg₂(dobpdc),⁵¹ Mn₂(dobpdc),⁵² Ni₂(dobpdc),⁵² Co₂(dobpdc),⁵² Zn₂(dobpdc),⁶¹ and Mg₂(dotpdc)⁵³ were prepared according to literature procedures (SI Section S1). Ultrahigh purity (>99.998%) gases were used for all adsorption experiments.

Infrared Spectra. Attenuated total reflectance (ATR) infrared (IR) spectra were collected on a PerkinElmer Spectrum 400 Fourier Transform (FT) IR spectrometer equipped with a Pike GladiATR and a home-built glovebag accessory used to control the atmosphere. Three vacuum-refill cycles were used to exchange the atmosphere of the glovebag accessory when preparing the system for in situ experiments. For humid FTIR spectra, samples were placed in 4 mL vials and sealed in a 20 mL vapor-dosing chamber containing ~4 mL of water. After at least 15 min of equilibration, the powder was removed, and spectra were collected. Co-adsorption of water in the sample was confirmed by observation of the H₂O IR vibrational bands at 1638 and 3350 (broad) cm⁻¹.⁶²

Diamine Grafting Procedure.⁵¹ A 20 mL scintillation vial was charged with toluene (4 mL) and 2-ampd (1 mL). Methanol-solvated Mg₂(dobpdc) (~15 mg) was filtered and washed with toluene (2 × 10 mL). (Note: Mg₂(dobpdc) should not be allowed to dry completely in air due to potential decomposition.⁴⁹) The filter-dried Mg₂(dobpdc) was added to the diamine solution, and the vial was swirled several times and allowed to stand at room temperature for at least 12 h. After this time, the mixture was filtered, and the resulting powder was washed with toluene (3 × 20 mL) and allowed to dry for ~3 min under reduced pressure, yielding ~25 mg of toluene-solvated 2-ampd-Mg₂(dobpdc). Other diamine-appended metal-organic frameworks described in this work were prepared using a similar procedure. Full characterization of all new diamine-appended frameworks prepared as part of this work, including PXRD patterns, IR spectra, dry N₂ thermogravimetric decomposition profiles, and CO₂ adsorption/desorption isobars, are included in the SI. Diamine loadings were determined by suspending ~5 mg of the diamine-appended metal-organic framework in 0.5 mL of DMSO-*d*₆ and then digesting the framework by adding several drops of DCl (35 wt % in D₂O) and heating until the mixture became homogeneous. The

resulting solutions were analyzed by ¹H NMR spectroscopy to determine the ratio of diamine to organic linker. Representative diamine loadings for all diamine-appended metal-organic frameworks prepared as part of this work are included in the SI.

Thermogravimetric Analysis and Cycling Measurements. Dry thermogravimetric analysis (TGA) experiments were conducted using a TA Instruments TGA Q5000. Humid TGA experiments were conducted using a TA Instruments TGA Q50. For humid experiments, the incident gas stream was passed through two room-temperature water bubblers in series, leading to an estimated water content of 2.6%, as determined by comparison to the water isotherms of 2-ampd-Mg₂(dobpdc) (Figure S11). Premixed cylinders of CO₂ in N₂ were obtained from Praxair. Samples were activated under flowing N₂ for 20–30 min until the mass stabilized; exact activation conditions for each diamine-appended material were determined through careful analysis of the dry N₂ thermal decomposition profiles and are included in the SI. Masses are uncorrected for buoyancy effects. A flow rate of 25 mL/min was used for all TGA experiments. Ramp rates for all isobaric measurements are included in figure captions. A ramp rate of 1.5 °C/min was employed for all dry N₂ decomposition experiments.

Gas Adsorption Measurements. Volumetric adsorption isotherms for N₂, O₂, and CO₂ were obtained using a Micromeritics ASAP 2020 gas adsorption analyzer. Adsorption isotherms for water were obtained using a Micromeritics 3Flex instrument. For water isotherms, the stainless-steel vapor dosing apparatus was subjected to three freeze-pump-thaw cycles to remove any dissolved gases, and heat tape was used to keep the exposed portion of the glass sample tube at elevated temperature to prevent condensation of water. The maximum relative humidity accessible in measurements with water was limited by the manifold temperature of 45 °C. Isotherms collected at 40, 50, and 60 °C were measured using a circulating water bath to control the sample temperature. Surface area measurements with N₂ were carried out at 77 K using a liquid N₂ bath. Samples were regenerated at 100 °C under reduced pressure (<10 μbar) for 2–4 h between isotherms. The isotherm data points were considered equilibrated after <0.01% change in pressure occurred over an average of 11 intervals of 15 s (for N₂, O₂, and CO₂) or 30 s (for H₂O).

Calculation of Differential Enthalpies and Entropies of Adsorption. Using a linear spline interpolation method and the CO₂ adsorption isotherms for 2-ampd-Mg₂(dobpdc) (Figure S7), the exact pressures (p_q) corresponding to specific CO₂ loadings (q) were determined at different temperatures (T). The Clausius-Clapeyron relationship (eq 1) was used to calculate the differential enthalpies of adsorption (Δh_{ads}) based on the slopes of the linear trendlines fit to $\ln(p_q)$ vs $1/T$ (Figure S8). The y -intercepts of these linear trendlines are equal to $-\Delta s_{\text{ads}}/R$ at each loading (assuming $p_0 = 1$ bar)⁶³ and thus were used to determine the corresponding differential entropies of adsorption (Figure S9).

$$\ln(p_q) = \left(\frac{\Delta h_{\text{ads}}}{R} \right) \left(\frac{1}{T} \right) + c \quad (1)$$

Breakthrough Measurements. See SI Section S11 for experimental details and SI figures.

Solid-State Magic Angle Spinning (MAS) NMR Experiments. Activation of 2-ampd-Mg₂(dobpdc) was carried out under flowing N₂ at 150 °C for 30 min. The activated material was packed into a 3.2 mm rotor inside a N₂-filled glovebag and further activated under vacuum inside a home-built gas manifold for 10 min at room temperature. This manifold has the key feature of enabling gas dosing of rotors at controlled pressures and subsequent sealing of dosed rotors prior to removal from the manifold.⁶¹ Samples were dosed with ¹³CO₂ gas (Sigma-Aldrich, 99 atom % ¹³C, < 3 atom % ¹⁸O) at room temperature (~22 °C) and allowed to equilibrate for 30 min prior to measurements, unless otherwise specified. For dosing with humid CO₂, a sample that had already been dosed with dry ¹³CO₂ was opened (the top and bottom rotor caps were removed), and the sample was placed in a gas stream of humid CO₂ (relative humidity 280

281 ~70%, measured using a ThermoPro TP50 Hygrometer) that was
 282 generated by flowing natural isotopic abundance CO₂ through a
 283 bubbler containing deionized water for 1 h.

284 All solid-state NMR experiments were carried out at 16.4 T using a
 285 Bruker 3.2 mm probe, and MAS rates were 15 kHz in all cases. All
 286 solid-state ¹³C NMR spectra were acquired by cross-polarization from
 287 ¹H (¹⁵N and ¹H contact RF field strengths of 20 kHz and 35 kHz,
 288 respectively). All cross-polarization experiments were acquired with
 289 continuous wave ¹H decoupling at 82 kHz RF field strength, and with
 290 the contact times stated in the figure captions. All ¹H NMR spectra
 291 were acquired using a 90° pulse-acquire sequence with a RF field
 292 strength of ~38 kHz, and recycle delays were adjusted to obtain
 293 quantitative spectra. The ¹H, ¹³C, and ¹⁵N chemical shifts were
 294 referenced to 1.8 ppm (adamantane), 38.5 ppm (adamantane tertiary
 295 carbon, left-hand resonance), and 33.4 ppm (glycine), respectively.⁶⁴

296 **Single-Crystal X-ray Diffraction.** Synthetic and experimental
 297 details for single-crystal X-ray diffraction experiments with 2-ampd-
 298 Zn₂(dobpdc) and molecular 2-ampd-CO₂ are included in SI Sections
 299 S12–S14.

300 **Density Functional Theory Calculations.** Our first-principles
 301 DFT calculations used a plane-wave basis and projector augmented-
 302 wave (PAW)^{65,66} pseudopotentials with the Vienna ab initio
 303 Simulation Package (VASP)^{67–70} code. To include the effect of the
 304 vdW dispersive interactions on binding energies and NMR chemical
 305 shifts, we performed structural relaxations with vdW dispersion-
 306 corrected functionals (vdW-DF2)⁷¹ as implemented in VASP. For all
 307 calculations, we used (i) a Γ -point sampling of the Brillouin zone
 308 (except for NMR calculations, as specified below), (ii) a 1000 eV
 309 plane-wave cutoff energy, and (iii) a 10^{−7} eV self-consistency
 310 criterion. We explicitly treat two valence electrons for Mg (3s²), six
 311 for O (2s²2p⁴), five for N (2s²2p³), four for C (2s²2p²), and one for H
 312 (1s¹). All structural relaxations were performed with a Gaussian
 313 smearing of 0.05 eV.⁷² The ions were relaxed until the Hellmann-
 314 Feynman forces were less than 0.001 eVÅ^{−1}. To compute CO₂ and
 315 H₂O binding energies, we optimized the structure of 2-ampd-
 316 Mg₂(dobpdc) prior to CO₂ and H₂O adsorption ($E_{\text{ampd-MOF}}$),
 317 interacting with CO₂ and H₂O in the gas phase ($E_{\text{CO}_2/\text{H}_2\text{O}}$) within
 318 a 15 × 15 × 15 Å³ cubic supercell, and 2-ampd-Mg₂(dobpdc) with
 319 adsorbed CO₂ and H₂O molecules ($E_{\text{CO}_2\text{-ampd-MOF}}$) using vdW-
 320 corrected DFT. The binding energies (E_B) were obtained via the
 321 difference:

$$322 \quad E_B = E_{\text{CO}_2\text{-ampd-MOF}} - (E_{\text{ampd-MOF}} + E_{\text{CO}_2/\text{H}_2\text{O}}) \quad (2)$$

323 For NMR simulations, we used a 1 × 1 × 3 k-point. With this k-point,
 324 the isotropic chemical shielding values (δ_{iso}) converged to 0.1 ppm.
 325 Since the isotropic chemical shift (δ_{iso}) is obtained from $\delta_{\text{iso}} = -(\delta_{\text{iso}} - \delta_{\text{ref}})$ where δ_{ref} is a reference value, we needed to determine a δ_{ref}
 326 value by comparing experimental δ_{iso} values to calculated δ_{iso} values.
 327 The σ_{ref} values for ¹H (31.4 ppm) and ¹³C (160.1 ppm) were
 328 obtained by first computing σ_{iso} values for cocaine (CSD refcode
 329 COCAIN10 was used as the starting point, and the structure was
 330 geometry optimized before NMR calculation; see SI for coordinates).
 331 The computed values were then compared with experimental values
 332 (Table S18, Figure S94).⁷³ The σ_{ref} value for ¹⁵N (215.9 ppm) was
 333 determined by comparison of DFT-calculated σ_{iso} and the
 334 experimental δ_{iso} value for glycine (Table S18).⁶¹ Additional DFT
 335 figures and details are included in SI Section S21.

337 ■ RESULTS AND DISCUSSION

338 **Adsorbent Design for NGCC Post-Combustion Cap-**
 339 **ture.** Our previous crystallographic and gas adsorption studies
 340 of 1°, 2° diamine-appended Mg₂(dobpdc) indicated that
 341 unfavorable chain-chain interactions in the *ab* plane of the
 342 framework give rise to the two-step adsorption profiles of these
 343 materials.⁵³ We reasoned that tethering the alkyl chain to the
 344 backbone of the diamine should alleviate these steric
 345 interactions, thereby minimizing the gap between the two
 346 CO₂ adsorption steps and enabling access to the full theoretical

adsorption capacity. Accordingly, we grafted racemic 2-
 (aminomethyl)piperidine (2-ampd, Figure 1b) to
 Mg₂(dobpdc) using our previously reported procedure⁵¹ to
 produce the adsorbent 2-ampd-Mg₂(dobpdc). Consistent
 with our hypothesis, this material exhibits two closely spaced
 steps in its CO₂ adsorption isotherms (occurring at 1.0 and 3.7
 mbar at 40 °C, respectively; see Figure 2). Importantly, both

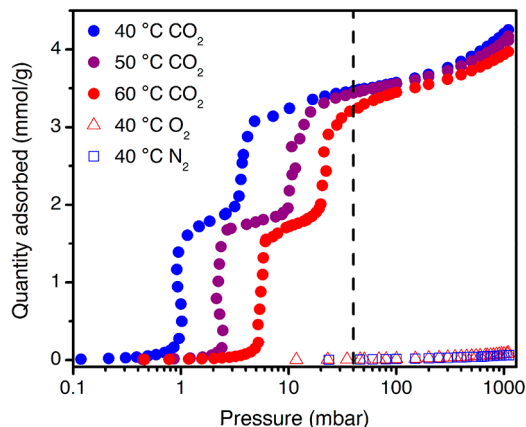


Figure 2. Pure CO₂ adsorption isotherms at 40, 50, and 60 °C (purple, blue, and red circles, respectively), and for O₂ (red triangles) and N₂ (blue squares) at 40 °C, for 2-ampd-Mg₂(dobpdc). The dashed black line indicates the approximate partial pressure of CO₂ in flue gas from a NGCC power plant (40 mbar).

steps occur at pressures low enough to facilitate ≥90% removal
 of CO₂ (residual pressure of ≤4 mbar) from NGCC flue
 emissions under idealized, equilibrium conditions at 40 °C. In
 contrast, variants of Mg₂(dobpdc) functionalized with
 diamines bearing long alkyl substituents, such as *N*-(*n*-
 hexyl)ethylenediamine (*n*Hex-2),⁵³ have two widely spaced
 CO₂ adsorption steps, restricting the quantity of CO₂ that can
 be captured to the capacity of the lower-pressure step (~1.8
 mmol/g at 40 mbar and 40 °C for *n*Hex-2, in contrast to 3.47
 mmol/g for 2-ampd under the same conditions; Figure S16).

We hypothesize that step-shaped CO₂ adsorption in 2-
 ampd-Mg₂(dobpdc) arises as a result of cooperative insertion
 of CO₂ into the metal-amine bonds to form chains of
 ammonium carbamate running along the pore axis, as reported
 previously for related alkylethylenediamine-appended frame-
 works.^{49–58} This conclusion is supported by spectroscopic
 characterization (discussed below) and by the observed metal
 dependence of the cooperative adsorption step position⁵⁰ for
 2-ampd-M₂(dobpdc) variants (M = Mg, Mn, Ni, Co, Zn; Figure
 S85). In addition, appending 2-ampd within the
 expanded terephenyl framework Mg₂(dotpdc) (dotpdc^{4−} =
 4,4′-dioxido-[1,1′:4′,1′′-terphenyl]-3,3′′-dicarboxylate) produ-
 ces an adsorbent with only one step in its CO₂ adsorption
 isobar (Figure S21), confirming that the two adsorption steps
 observed for 2-ampd-Mg₂(dobpdc) also arise from steric
 interactions between adjacent diamines in the framework (SI
 Section S4). Importantly, 2-ampd-Mg₂(dobpdc) possesses
 comparable or superior thermal stability to all other 1°/2°
 diamine-appended variants of Mg₂(dobpdc) evaluated to date
 (Figure S6), withstanding 12 h of exposure to flowing, humid
 CO₂ at a regeneration temperature of 140 °C (or even as high
 as 180 °C) with minimal diamine volatilization (Table S15, see
 also discussion below). Therefore, the cyclic diamine 2-ampd
 uniquely affords the best attributes achieved with 1°/2°

diamine-appended $\text{Mg}_2(\text{dobpdc})$ materials to date, namely, high thermal stability coupled with a high CO_2 adsorption capacity from a NGCC flue gas stream.

The single crystal X-ray diffraction structure of the isostructural framework 2-ampd- $\text{Zn}_2(\text{dobpdc})$ (Figure 1) provides insight into the thermal stability and close CO_2 adsorption steps of 2-ampd- $\text{Mg}_2(\text{dobpdc})$. The bulky piperidine ring of 2-ampd can maintain a stable chair conformation in the pores of the framework, with efficient packing in the *ab* plane and minimization of unfavorable interactions between adjacent diamines. Consistently, despite the high density of amine groups within the pores, 2-ampd- $\text{Mg}_2(\text{dobpdc})$ exhibits a high Brunauer–Emmett–Teller surface area of $618 \pm 2 \text{ m}^2/\text{g}$ (Figure S4), which should enable rapid diffusion of CO_2 through the channels of the framework, even after CO_2 adsorption.

Single-Component Adsorption Experiments. Following validation of these initial design criteria, we investigated additional properties relevant to the application of 2-ampd- $\text{Mg}_2(\text{dobpdc})$ in CO_2 capture from NGCC flue emissions. Isothermal adsorption profiles were collected at 40, 50, and 60 °C for CO_2 and at 40 °C for N_2 and O_2 (Figure 2). For CO_2 , two adsorption steps were observed at all temperatures. Both adsorption steps occur below 40 mbar even at 60 °C and are predicted to be operative in this target pressure range up to approximately 69 °C (Figure S14). Importantly, because 2-ampd- $\text{Mg}_2(\text{dobpdc})$ adsorbs minimal CO_2 at partial pressures beneath the first step pressure, processes with higher adsorption temperatures can be considered without sacrificing CO_2 adsorption capacity, as would be expected for a typical Langmuir-type adsorbent. Eliminating the need to adsorb at the lowest possible temperature can potentially reduce process costs through relaxed requirements for flue gas cooling,⁷⁴ minimization of water coadsorption,⁴⁷ and/or enhanced tolerance to temperature rise in the adsorbent bed upon exothermic CO_2 adsorption.²¹ In addition, despite demonstrating strong adsorption of CO_2 at low partial pressures, 2-ampd- $\text{Mg}_2(\text{dobpdc})$ can be fully regenerated by heating to only 140 °C under a flow of dry or humid CO_2 at atmospheric pressure (Figure S37). Furthermore, at the partial pressures relevant to natural gas flue emissions, 2-ampd- $\text{Mg}_2(\text{dobpdc})$ demonstrates excellent noncompetitive CO_2/N_2 and CO_2/O_2 selectivities of 1320 and 694, respectively (Table S1), which are among the highest reported for a nonsize-selective metal–organic framework.^{31,35,75–78} Because N_2 and O_2 cannot participate in the CO_2 -selective cooperative adsorption mechanism, these values are anticipated to be reflective of the multicomponent performance of the material.

The thermodynamics of CO_2 adsorption in 2-ampd- $\text{Mg}_2(\text{dobpdc})$ were analyzed using the data in Figure 2. A spline interpolation method was used to calculate lines of constant loading for the set of CO_2 isotherms from 40 to 60 °C. Employing the Clausius–Clapeyron relationship yielded a differential enthalpy of adsorption (Δh_{ads}) of $-73 \pm 2 \text{ kJ/mol}$ at a loading of 1 mmol/g (Figure S8), similar to that observed for other diamine-appended variants of $\text{Mg}_2(\text{dobpdc})$ ^{50–52} and smaller in magnitude than the low-coverage enthalpies reported for silicas functionalized with primary or secondary amines.⁷⁹ From this adsorption enthalpy, we calculated a projected regeneration energy of 2.8 MJ/kg CO_2 for a temperature swing adsorption (TSA) process consisting of capture from a 40 mbar stream of CO_2 at 40 °C and desorption under 1 bar of CO_2 at 140 °C (see SI Section S3;

note that only CO_2 was considered in this calculation). This value is over 30% lower than the regeneration energy projected for a polyamine-functionalized silica for a similar process (3.9 MJ/kg CO_2 , see SI Section S3),⁴⁸ reflecting the advantage of cooperative adsorbents for CO_2 capture applications. Furthermore, with a higher adsorption temperature of 60 °C, an even lower projected regeneration energy of 2.7 MJ/kg CO_2 may be possible for 2-ampd- $\text{Mg}_2(\text{dobpdc})$ (considering only CO_2 ; see Table S2). Notably, the thermodynamics of adsorption for 2-ampd- $\text{Mg}_2(\text{dobpdc})$ were found to adhere to the same enthalpy–entropy correlation as other diamine-appended variants of $\text{Mg}_2(\text{dobpdc})$ ⁵¹ (Figure S15), corroborating the formation of ammonium carbamate chains upon CO_2 adsorption in this material.

Mixed-Gas Adsorption Experiments. While single-component equilibrium data are needed to guide adsorbent design and characterize fundamental adsorption properties, multicomponent experiments are critical to evaluate adsorbent performance under more realistic process conditions. To that end, we performed extensive dry and humid thermogravimetric experiments with 2-ampd- $\text{Mg}_2(\text{dobpdc})$ using CO_2/N_2 mixtures and simulated NGCC flue emission streams. When exposed to a flow of dry simulated NGCC flue gas (4% CO_2 in N_2) at atmospheric pressure, 2-ampd- $\text{Mg}_2(\text{dobpdc})$ exhibits a high CO_2 capacity of 16.0 g/100 g (3.63 mmol/g) at 40 °C (Figure 3a, purple curve), consistent with the predicted capacity of 3.66 mmol/g for adsorption of 1 CO_2 per diamine. This adsorption capacity is significantly higher than that of other cyclic diamine-appended variants of $\text{Mg}_2(\text{dobpdc})$ (2.02–2.33 mmol/g, Figure S30), as well as the representative amine-functionalized silica MCM-41-PEI-50^{80,81} (1.48 mmol/g, Figure S79) under equivalent conditions. However, for a dry 0.4% CO_2 in N_2 stream, representing the lowest adsorption pressure (4 mbar CO_2) required for 90% capture of CO_2 from NGCC emissions, the adsorption capacity at 40 °C (2.81 g/100 g, or 0.639 mmol/g, Figure 3a) is significantly lower than that observed in the 40 °C pure CO_2 isotherm at the same CO_2 partial pressure (2.76 mmol/g). Even with extremely slow isobaric cooling rates, similar discrepancies in the threshold conditions for cooperative adsorption have been observed between CO_2 adsorption isobars (collected under flowing CO_2/N_2 mixtures) and volumetric isotherms (collected under pure CO_2 starting from vacuum).^{82,83} In general, the isobaric measurements show lower isobaric step temperatures (equivalent to higher isothermal step pressures) than would be expected given the measured equilibrium adsorption isotherms. These results suggest a smaller thermodynamic driving force for CO_2 capture under the more realistic, mixed-gas flow conditions. Additionally, we found that the adsorption capacity decreased when a faster cooling ramp rate (0.2 versus 0.1 °C/min) was employed, suggesting that the adsorption kinetics are limited in streams with low CO_2 partial pressures (SI Section S9). This result is consistent with a previous report investigating the adsorption kinetics of the related material mmen- $\text{Mg}_2(\text{dobpdc})$ (mmen = *N,N'*-dimethylethylenediamine).⁸⁴ Ultimately, thermodynamic and kinetic factors under process-relevant flow conditions indicate that 2-ampd- $\text{Mg}_2(\text{dobpdc})$ falls short of achieving the target of $\geq 90\%$ CO_2 capture from NGCC flue gas under dry conditions.

We also analyzed the ability of 2-ampd- $\text{Mg}_2(\text{dobpdc})$ to capture CO_2 in the presence of water, which can constitute up to ~8% of NGCC flue gas by volume. Humid isobars were collected by flowing CO_2/N_2 mixtures through two room-

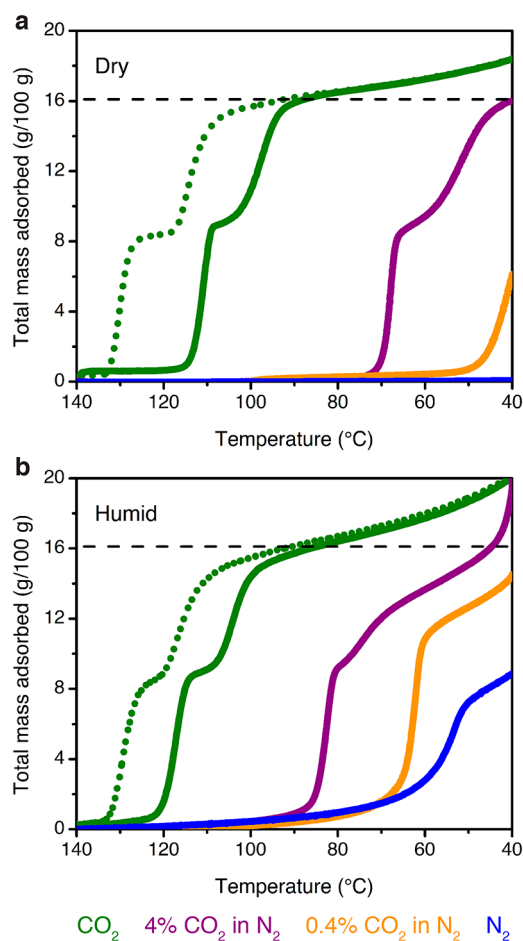


Figure 3. Dry (a) and humid (b, ~2.6% H₂O) isobars at atmospheric pressure for pure CO₂ (green), 4% CO₂ in N₂ (purple), 0.4% CO₂ in N₂ (orange), and pure N₂ (blue) in 2-ampd-Mg₂(dobpdc). Solid lines depict adsorption (cooling), and dotted green lines depict desorption (heating) for the pure CO₂ isobars. The dashed black lines indicate the theoretical capacity for adsorption of 1 CO₂ per diamine. Temperature ramp rates: 0.5 °C/min for pure CO₂, 0.1 °C/min for 4% and 0.4% CO₂ in N₂, and 1 °C/min for pure N₂.

Figure 3b). However, at lower temperatures, the saturation capacities of the humid CO₂/N₂ mixture isobars exceed the gravimetric uptake anticipated for adsorption of 1 CO₂ per diamine, suggesting coadsorption of water. In summary, the isobaric adsorption data indicate that while 2-ampd-Mg₂(dobpdc) may fall below the target of ≥90% CO₂ capture from dry NGCC flue emissions, the presence of humidity in the gas stream should enable the material to reach this target at temperatures up to at least 60 °C.

To quantify the influence of water on the thermodynamics of CO₂ capture, approximate CO₂ adsorption enthalpies were calculated for the dry and humid CO₂/N₂ mixture isobars by employing the Clausius–Clapeyron relationship at the midpoint of each adsorption step. We note that while slow temperature ramp rates were used to approximate equilibrium conditions (SI Section S9), the enthalpies calculated from the adsorption isobars were found to be systematically higher than those calculated from the single-component, volumetric isotherms. Nonetheless, the difference between the humid and dry isobar enthalpies ($\Delta h_{\text{ads,humid}} - \Delta h_{\text{ads,dry}}$) should reflect the enthalpic benefit of CO₂ adsorption in the presence of water. Using this method, we attribute the increased temperature of the first adsorption step to a 31 ± 2 kJ/mol increase in the effective $-\Delta h_{\text{ads}}$ in the presence of water (dry: 81 ± 1 kJ/mol; humid: 112 ± 2 kJ/mol). Notably, within error, the same increase in effective $-\Delta h_{\text{ads}}$ was found for the lower-temperature adsorption step (30 ± 2 kJ/mol), indicating that water uniformly increases the thermodynamic driving force for both adsorption steps (Tables S7 and S8). Interestingly, minimal change was observed in the isobaric desorption step temperatures following saturation with CO₂/H₂O under the tested humidity, resulting in calculation of equivalent enthalpies within error (dry: 101 ± 1 kJ/mol; humid: 99 ± 1 kJ/mol; difference: -2 ± 2 kJ/mol). While these results are complicated by the lower relative humidities at the elevated desorption temperatures, the similar dry and humid CO₂ desorption step temperatures suggest that water desorbs before CO₂.

In order to quantify the influence of water on the performance of 2-ampd-Mg₂(dobpdc), we collected single-component water adsorption isotherms at 30, 40, 50, and 60 °C. For all temperatures, the isotherms show a plateau at a loading of 1 H₂O per diamine, followed by condensation at higher relative humidities (Figures S10 and S11). Using the same spline interpolation method as for CO₂, a differential adsorption enthalpy of -65 ± 2 kJ/mol was calculated at a loading of 1 mmol H₂O/g (Figure S12). Assuming coadsorption and desorption cycling of 1 water molecule per diamine-Mg²⁺ site alongside cycled CO₂, the regeneration energy of 2-ampd-Mg₂(dobpdc) would increase by up to 1.5 MJ/kg CO₂ to a total of 4.3 MJ/kg CO₂ (SI Section S3). We note that these values are only approximations, as they do not account for potential differences in the adsorption enthalpy of water on the CO₂-inserted and diamine-bound phases (see DFT calculations below), the potential effect of higher relative humidity levels on adsorption or desorption, and the relative adsorption/desorption kinetics of CO₂ vs H₂O in the ultimate cycling configuration. Nonetheless, 2-ampd-Mg₂(dobpdc) is still predicted to afford significant energy savings over competing amine-based technologies such as a PEI-functionalized silica, which requires a regeneration energy of 4.7 MJ/kg CO₂ under similar conditions (SI Section S3)⁴⁸ and is susceptible to degradative reaction pathways, such as urea

599 formation (Figures S74–S77, discussed in greater detail
600 below). Therefore, while these measurements indicate that
601 the presence of water in the incident gas stream improves the
602 thermodynamic driving force for CO₂ adsorption in 2-ampd–
603 Mg₂(dobpdc), this improvement comes at the potential cost of
604 an increase in the regeneration energy associated with the
605 desorption of coadsorbed water. The cocycled water would
606 then need to be condensed prior to compression and transport
607 of the captured CO₂.

608 **Fixed-Bed Adsorption Experiments.** To evaluate the
609 performance of 2-ampd–Mg₂(dobpdc) in a fixed-bed
610 adsorption process, we conducted breakthrough experiments
611 under dry and humid simulated NGCC flue gas. These
612 experiments are particularly important for materials with step-
613 shaped isotherms, which often give rise to complex, multi-
614 modal breakthrough profiles. Such profiles were originally
615 anticipated for diamine-appended frameworks by Mazzotti and
616 co-workers in a comprehensive modeling study,⁴⁵ and a review
617 of the underlying theory is included in SI Section S10. In short,
618 the breakthrough profile can be predicted from an isotherm
619 with one or more inflection points by applying “Golden’s
620 Rule,” alternatively known as the rubber band rule or string
621 rule.^{45,85–87} When applying this rule, an operating curve for
622 adsorption is constructed by stretching a hypothetical “rubber
623 band” beneath the adsorption isotherm from the initial state
624 (0% CO₂) to the feed state (4% CO₂). In concentration
625 regimes bounded by individual points of contact with the
626 rubber band, a compressive “shock” is anticipated in the
627 breakthrough profile. In concentration regimes where the
628 rubber band runs along the isotherm, a dispersive “wave” is
629 expected. With a step-shaped isotherm, the result is often a
630 “shock–wave–shock” profile: an initial “shock” is generated as
631 CO₂ slips through the bed at concentrations beneath the step,
632 followed by a “wave” corresponding to a small increase in CO₂
633 concentration during the onset of the cooperative adsorption
634 step, and finally a second “shock” at full breakthrough (see
635 Figure S52). Intuitively, the shock–wave–shock profile can be
636 understood as a manifestation of the general inability of a
637 cooperative adsorbent to capture CO₂ once the CO₂ partial pressure
638 in the bed drops below the step pressure. Accordingly, this
639 behavior is the basis for our design criterion to achieve 90%
640 capture of CO₂ through the selection of adsorbents with step
641 pressures at <10% of the feed concentration.⁵¹

642 Breakthrough experiments were conducted with 0.73 g of
643 semispherical pellets of 2-ampd–Mg₂(dobpdc) (350–700 μm)
644 under 28 sccm of 4% CO₂ in N₂ at 1.1 bar (Figure 4; details of
645 pellet preparation and characterization are given in SI Section
646 S11). Considering the single-component CO₂ adsorption
647 isotherms, a CO₂ “slip” (initial shock) of ~0.02 mol % was
648 predicted under dry flue gas at 40 °C (obtained from Golden’s
649 Rule, see Figure S54), corresponding to a capture rate of 99.5%
650 from a stream containing 4% CO₂ (calculated as $(1 - 0.02/4) \times$
651 100%). However, with dry simulated flue gas, approximately
652 0.6 mol % CO₂ slip was detected at the outlet, corresponding
653 to a lower maximum capture rate of 86%. In addition, the CO₂
654 capacity at exhaustion (full breakthrough) was found to be 2.4 ± 0.2
655 mmol/g, which fell short of the capacity of 3.5 mmol/g
656 predicted from the adsorption isotherm. The breakthrough
657 profile and capacity were highly reproducible following
658 activation of the material at 120 °C under flowing He (Figure
659 S55). Reducing the flow rate to 14 sccm at 40 °C improved the
660 capture rate (~0.4 mol % slip, or 90% capture rate) and
661 sharpness of the breakthrough profile, reflecting a potential

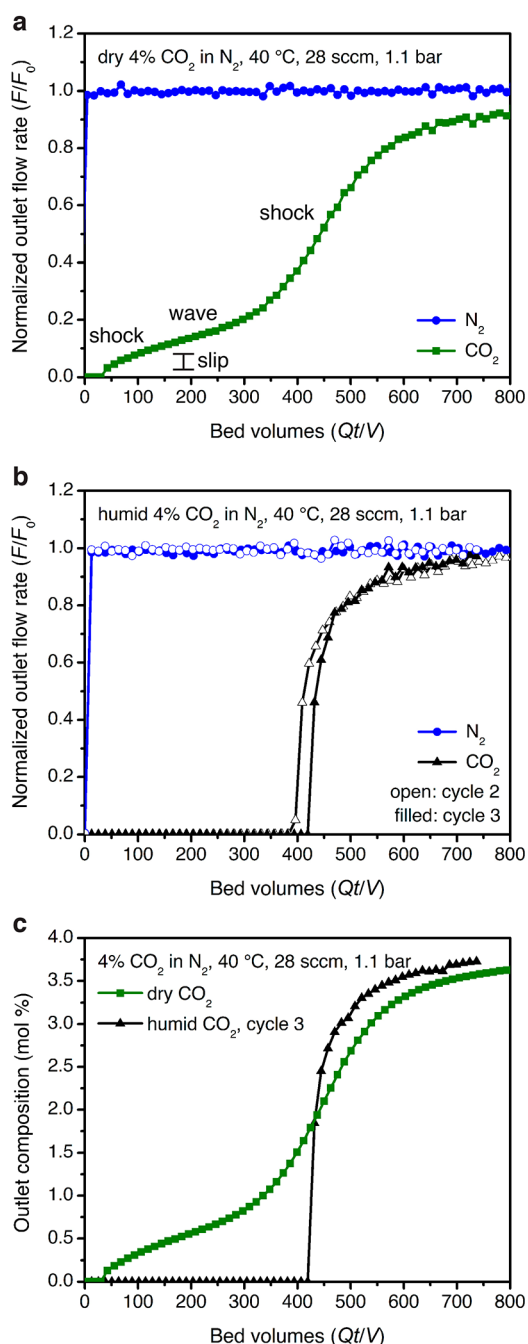


Figure 4. Breakthrough experiments with 2-ampd–Mg₂(dobpdc) under 28 sccm of a simulated NGCC flue emission stream of 4% CO₂ in N₂ at 40 °C and ~1.1 bar. (a) Experiment with dry simulated flue gas. Capture rate: 86%; exhaustion capacity: 2.4 ± 0.2 mmol/g. (b) Second (filled symbols) and third (open symbols) breakthrough experiment cycles with humid flue gas following presaturation of the adsorbent bed with water. Capture rate: > 99%; usable capacity (average ≥90% capture): 2.2 and 2.3 ± 0.1 mmol/g; exhaustion capacity: 2.4 and 2.5 ± 0.1 mmol/g for 2nd and 3rd cycles, respectively. (c) Overlay of dry and humid (3rd cycle) CO₂ breakthrough profiles. The y-axis is shown as normalized outlet flow rate (F/F_0) in (a) and (b) and as outlet composition in mol % in (c).

limitation in kinetics, but the breakthrough capacity at 662 exhaustion remained unchanged (Figure S56). As anticipated 663 from the isotherms and isobars, increasing the temperature to 664 60 °C increased the CO₂ slip, resulting in a measured capture 665 rate of only 62% (Figure S57; predicted capture rate, 88%). 666

The CO₂ breakthrough capacity at exhaustion was calculated as 2.2 ± 0.2 mmol/g, which again fell short of that predicted from the isotherm (3.2 mmol/g) but was consistent with that predicted from the CO₂ mixture isobars (2.2 mmol/g). Therefore, these results suggest that isobars collected by flowing dry CO₂ mixtures (Figure 3a) may reflect adsorbent performance in dry breakthrough measurements more accurately than single-component, volumetric isotherms (Figure 2). We anticipate that the greater utility of mixed-gas isobars versus single-component isotherms will apply generally in the evaluation of other carbon capture materials, particularly those with step-shaped adsorption isotherms.

To test the effect of CO₂ concentration on the elution profile, a breakthrough experiment was conducted under 14 sccm of 15% CO₂ in N₂ at 40 °C and atmospheric pressure, simulating coal flue gas (Figure S58). In this experiment, negligible slip was observed (>99% CO₂ capture), and the CO₂ capacity (3.1 ± 0.2 mmol/g) was consistent with that of the equilibrium isotherm (3.6 mmol/g), considering the 92% diamine loading of the pellets. Therefore, the deviations from equilibrium behavior observed in breakthrough experiments with lower CO₂ concentrations (Figure 4), particularly with respect to high CO₂ slip and resulting low CO₂ capture rate, can likely be attributed to limitations in kinetics. As a result, nonequilibrium effects may limit the performance of diamine-appended frameworks with dry CO₂ mixtures at low partial pressures, a hypothesis supported by a recent investigation of another diamine-appended framework for CO₂ capture from air.⁸⁴

We also evaluated the breakthrough behavior of the material under humid flue gas mixtures containing ~2 vol % H₂O. Gratifyingly, consistent with the humid isobar measurements (Figure 3b), a dramatic enhancement in CO₂ capture performance was observed in breakthrough experiments with humid simulated NGCC flue gas following presaturation of the adsorbent bed with water (Figure 4b). In particular, humidification completely eliminated the initial CO₂ slip at 40 °C, resulting in a CO₂ capture rate of >99% and a desirable single, sharp CO₂ breakthrough front. The CO₂ exhaustion capacity calculated at full breakthrough (2.4 ± 0.2 mmol/g) was equivalent to that of the dry experiment, with a usable CO₂ capacity of 2.2 ± 0.1 mmol/g satisfying the DoE target of an average of 90% CO₂ capture. This striking improvement in performance is clearly visible in an overlay of the dry and humid CO₂ breakthrough profiles at 40 °C (Figure 4c). Breakthrough experiments at 60 °C revealed similarly dramatic improvements in performance upon addition of humidity (Figures S59 and S60), with an increase in capture rate from 62% to >99% (see Table S11 for a summary of capture rate results). The very high capture rate under humid conditions at 60 °C suggests that even higher adsorption temperatures could be used to achieve smaller temperature swings. In ongoing work, we are developing methods to predict the breakthrough performance as a function of both relative humidity and temperature. The promising performance of 2-ampd-Mg₂(dobpdc) in humid breakthrough experiments supports its utility as a next-generation adsorbent for postcombustion CO₂ capture from NGCC flue emissions.

Influence of Water on CO₂ Adsorption. Due to the sensitivity of the adsorption threshold to the local environment in cooperative adsorbents, it is of interest to determine whether the presence of water changes the nature of the chemisorbed phase or merely enhances the thermodynamic favorability of

the ammonium carbamate chain mechanism in diamine-appended metal-organic frameworks. Considering related materials, water is well-known to improve the CO₂ adsorption capacity of amine-functionalized silicas.^{30,42,88–99} This effect is generally ascribed to a mechanistic shift from ammonium carbamate formation (0.5 CO₂:amine) to bicarbonate or stabilized carbamic acid formation (1 CO₂ per amine),^{12,89–91,95,96,99–108} although some studies have debated the formation of bicarbonates or carbonates.^{109–112} Furthermore, these reports largely focus on the influence of water on the adsorption capacity, with minimal discussion of the influence of water on the thermodynamics of adsorption and the desorption temperature.^{89,92,113,114} Notably, our related vdW-corrected DFT study of the framework mmen-Mg₂(dobpdc) demonstrated a stabilization of up to 41 kJ/mol for the CO₂-inserted phase in the presence of water.¹¹⁵ This result suggests that water enhances, rather than changes, the ammonium carbamate chain adsorption mechanism, but to date no study has yet combined experimental and computational methods to characterize the effect of water on the CO₂ adsorption pathway, capacity, and breakthrough profile of a diamine-appended metal-organic framework. Accordingly, we employed IR and NMR spectroscopy and vdW-corrected DFT calculations to probe the behavior of 2-ampd-Mg₂(dobpdc) under dry and humid conditions.

We first collected IR spectra of 2-ampd-Mg₂(dobpdc) in the presence of dry N₂, dry CO₂, and humid CO₂ (Figure 5).

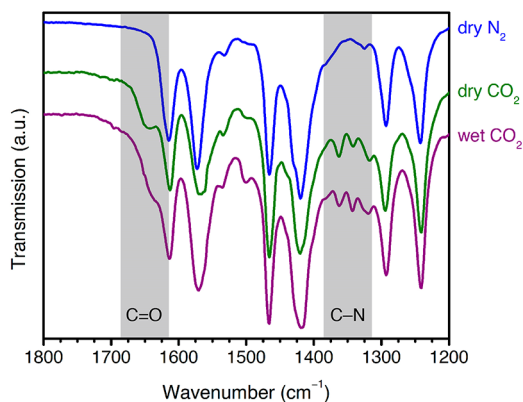


Figure 5. Infrared spectra of 2-ampd-Mg₂(dobpdc) under dry N₂ (blue), dry CO₂ (green), and humid CO₂ (purple) at room temperature (~22 °C) and atmospheric pressure. The C(O)O[−] vibration at 1648 cm^{−1} and C–N//N–C(O)O[−] vibrations at 1362 and 1342 cm^{−1} are consistent with the proposed mechanism of ammonium carbamate chain formation under both dry and humid conditions.

Upon exposure to dry CO₂ at 22 °C and atmospheric pressure, broad C(O)O[−] (1648 cm^{−1}) and sharp C–N//N–C(O)O[−] (1362 and 1342 cm^{−1}) vibrations were observed, consistent with the anticipated ammonium carbamate chain mechanism.¹¹⁴ Similar new vibrations were observed at 1637 and 1340 cm^{−1} in the IR spectrum of the molecular ammonium carbamate 2-ampd–CO₂ compared to the spectrum of free molecular 2-ampd (Figures S61–S63; crystallographic data provided as SI). We note that the reported C(O)O[−] stretches are shifted to higher energies compared to those generally assigned to carbamates in amine-functionalized silicas (1500–1600 cm^{−1}),¹¹⁴ which we attribute to the strong hydrogen bonding between the ammonium and carbamate units in these

770 materials. The presence of two C–N/N–C(O)O[−] stretches in
 771 the IR spectrum of CO₂-dosed 2-ampd–Mg₂(dobpdc) further
 772 suggests the formation of two distinct ammonium carbamate
 773 products upon CO₂ adsorption. The C–N/N–C(O)O[−]
 774 vibrations persist in the presence of humid CO₂, consistent
 775 with preservation of a chemisorptive mechanism, while the
 776 C(O)O[−] band is obscured by the H–O–H bend at 1630 cm^{−1}
 777 arising from coadsorbed water.¹⁰²

778 Solid-state NMR spectra obtained under dry and humid
 779 conditions provided greater experimental detail for the effect of
 780 water on CO₂ adsorption in 2-ampd–Mg₂(dobpdc) (Figure
 781 6). The ¹³C NMR spectrum of 2-ampd–Mg₂(dobpdc) dosed

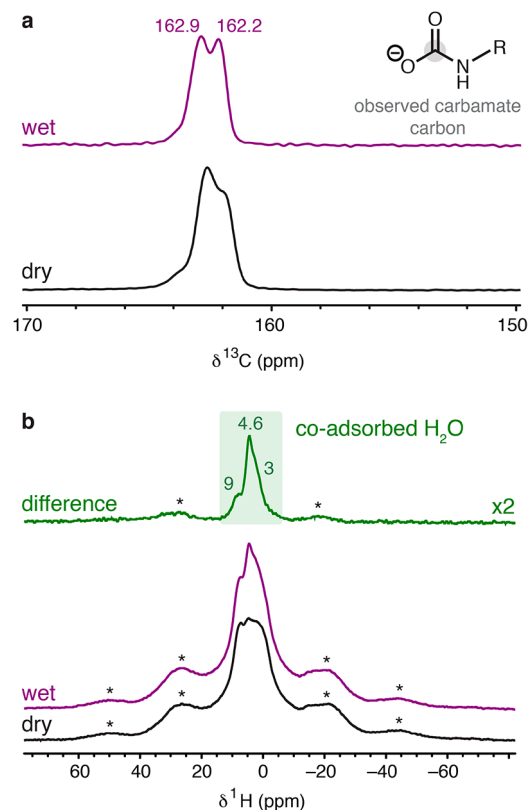


Figure 6. (a) ¹³C NMR (16.4 T) MAS spectra of 2-ampd–Mg₂(dobpdc) dosed with 1025 mbar of dry ¹³CO₂ at 22 °C (bottom), and the same sample under a subsequent flow of humid, natural isotopic abundance CO₂ at atmospheric pressure (top). Spectra were obtained by cross-polarization from ¹H (contact time = 1 ms). Peaks corresponding to the framework linker are not observed due to the low natural abundance of ¹³C nuclei in the framework compared to the 99% ¹³C enrichment level for the chemisorbed CO₂. (b) ¹H NMR spectra obtained by single-pulse excitation for the same samples as in (a). The MAS rate was 15 kHz in all cases. Asterisks mark spinning sidebands.

782 with 1025 mbar of ¹³CO₂ at room temperature shows two
 783 predominant overlapping resonances at 162 and 163 ppm, as
 784 well as a weak shoulder at a higher chemical shift (Figure 6a),
 785 all of which can be ascribed to chemisorbed CO₂ species. (See
 786 Figure S87 for the ¹³C spectrum of activated 2-ampd–
 787 Mg₂(dobpdc) prior to exposure to CO₂.) We hypothesize that
 788 the two main ¹³C resonances (Figure 6a) correspond to two
 789 conformations of ammonium carbamate chains,⁶¹ consistent
 790 with the IR spectrum collected under dry CO₂ (Figure 5).
 791 Notably, our previous NMR characterization of diamines
 792 exhibiting double-step CO₂ adsorption profiles also revealed

multiple resonances for chemisorbed CO₂, which likely arise
 due to spectroscopically distinct conformations of the sterically
 hindered ammonium carbamate chains.⁶¹ The weak shoulder
 at higher frequencies (Figure 6a) may be associated with
 incomplete equilibration (see Figure S90).

To interpret these results, we carried out additional 2D and
¹⁵N NMR experiments. A ¹H–¹³C HETCOR experiment with
 a short contact time (100 μs) was performed to probe
 correlations with hydrogen atoms that are proximal to the
 chemisorbed carbon species (i.e., within a few Å; Figure S89).
 In the 2D experiment, the two ¹³C resonances each show a
 major ¹H correlation at ~5 ppm. We assign this feature to the
 N–H group of an ammonium carbamate species, while the ¹³C
 peaks are attributed to the carbamate carbon atoms of two
 distinct conformations of ammonium carbamate chains.^{61,116}
 The observed single N–H correlation supports CO₂ insertion
 into metal–1° amine bonds to produce metal-bound
 carbamate species, with proton transfer to neighboring
 secondary amines to form charge-balancing ammonium
 groups. This reactivity is consistent with the previous
 crystallographic characterization of CO₂ insertion into
 Zn₂(dobpdc) functionalized with 1°/2° diamines.⁵¹ Additionally,
 the ¹⁵N NMR spectrum of 2-ampd–Mg₂(dobpdc) dosed
 with 1025 mbar of ¹³CO₂ featured two peaks at 46 and 76
 ppm, consistent with nitrogen atoms in ammonium and
 carbamate groups, respectively (Figure S86).^{50,61}

After exposure of 2-ampd–Mg₂(dobpdc) to a flow of humid
 CO₂ (natural isotopic abundance) for 1 h, the main two ¹³C
 resonances were retained, but smaller line widths were
 observed (Figure 6a; see also Figure S90 for similar data
 obtained with a longer CO₂ exposure time). Therefore, in
 further agreement with the IR data, these NMR spectra
 demonstrate retention of the ammonium carbamate product in
 the presence of water and exclude a water-induced change in
 the CO₂ chemisorption mechanism. Co-adsorption of water
 was also confirmed by collection of ¹H NMR spectra before
 and after exposure to wet CO₂. The difference ¹H spectrum
 (Figure 6b) shows positive intensity that can be attributed to
 coadsorbed water and reveals a narrow component at 4.6 ppm,
 as well as broad components at ~9 and ~3 ppm. The highly
 shifted (~9 ppm) water peak supports the formation of strong
 hydrogen bonds following exposure to water (Figure 6b).
 Additionally, the ¹H NMR spectra of 2-ampd–Mg₂(dobpdc)
 following exposure to dry or humid CO₂ (Figure 6b) show an
 increase in line width of the amine resonances compared to the
 NMR spectrum of activated 2-ampd–Mg₂(dobpdc) (Figure
 S88), consistent with a reduction of amine mobility following
 CO₂ insertion.

Due to the structural complexity of 2-ampd–Mg₂(dobpdc),
 the CO₂-inserted structure could not be solved directly from
 the X-ray diffraction pattern of the microcrystalline powder or
 from single crystals of the isostructural Zn framework under
 dry or humid conditions. We thus turned to vdW-corrected
 DFT calculations to predict the structure and energetics upon
 CO₂ adsorption, H₂O adsorption, and coadsorption of CO₂
 and H₂O in 2-ampd–Mg₂(dobpdc) (Figure 7). For simplicity,
 all calculations were carried out using the left-handed
 enantiomer of the diamine in the right-handed enantiomer of
 the framework. An adsorption energy of −70 kJ/mol was
 calculated for insertion of CO₂ to form ammonium carbamate
 chains in Mg₂(dobpdc)(2-ampd–CO₂)₂. This value is in good
 agreement with the experimentally determined CO₂ adsorption
 enthalpy of −72 ± 5 kJ/mol averaged over a loading of 0 to 1

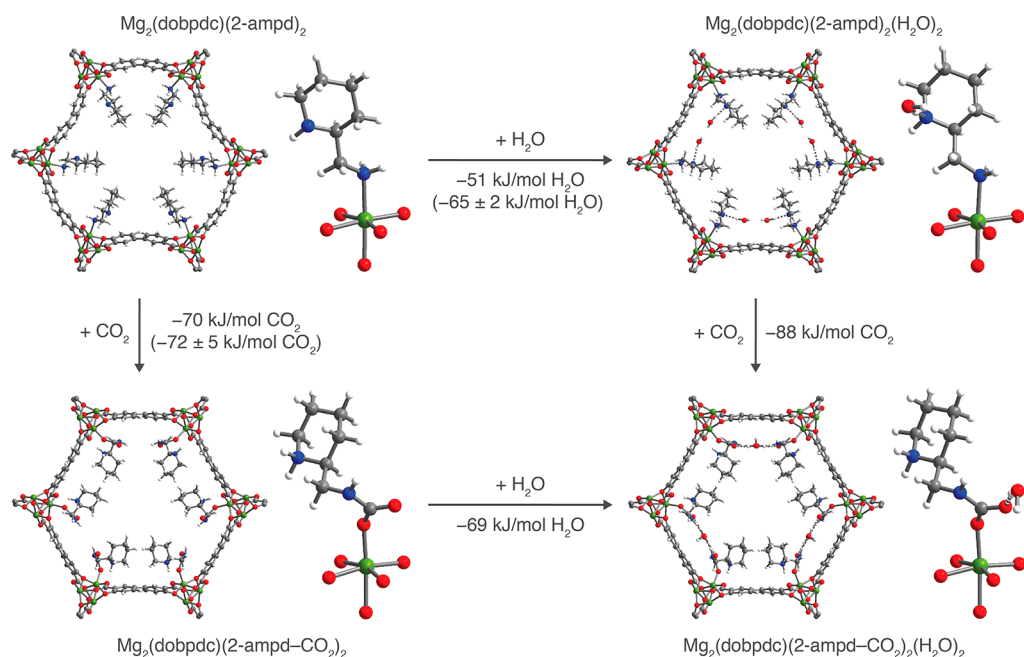


Figure 7. Projections along the pore axis and first coordination spheres of Mg(II) sites for the vdW-corrected, DFT-calculated structures of evacuated *L*-2-ampd-*R*-Mg₂(dobpdc) (top left) and the framework following CO₂ insertion (bottom left), water adsorption (top right), and coadsorption of CO₂ and H₂O (bottom right). The vdW-corrected, DFT-calculated binding energies (ΔE) are provided for each adsorption process, and available experimental differential binding enthalpies (Δh_{ads}) are included in parentheses. Co-adsorption of water was found to enhance the CO₂ binding energy by -18 kJ/mol, and a combined binding energy of -139 kJ/mol 2-ampd was calculated for coadsorption of 1 CO₂ and 1 H₂O per diamine. Green, blue, gray, red, and white spheres represent Mg, N, C, O, and H atoms, respectively.

CO₂ per diamine (Figure S8). In the calculated structure of Mg₂(dobpdc)(2-ampd)₂(H₂O)₂, adsorbed water was found to interact with 2-ampd by donating a hydrogen bond to the secondary amine (O...N distance of 2.924 Å). Close H₂O...H₂O contacts in the *ab* plane (O...O distance of 2.867 Å) suggest that additional stabilization is provided by hydrogen bonding between water molecules. In the absence of CO₂, an adsorption energy of -51 kJ/mol was calculated for H₂O. This value is consistent with the experimental H₂O adsorption enthalpy of -50 ± 2 kJ/mol at low loadings (0.2 mmol/g, or 0.05 mmol H₂O per diamine) but is slightly lower than the average experimental enthalpy of -65 ± 2 kJ/mol over a loading range of 0 to 1 mmol H₂O per diamine (Figure S12). In practice, while the structure shown here represents the lowest-energy H₂O binding mode discovered in our 0 K calculations, H₂O may sample other binding sites or geometries within the pore at room temperature. Overall, the adsorption energies corresponding to the calculated CO₂- and H₂O-adsorbed structures of 2-ampd-Mg₂(dobpdc) are in reasonable agreement with those determined from single-component adsorption measurements.

The DFT-calculated structure of Mg₂(dobpdc)(2-ampd-CO₂)₂(H₂O)₂ shows a strong hydrogen bonding interaction between H₂O and the metal-bound oxygen atom of the carbamate (O...O distance of 2.786 Å). Additionally, each H₂O molecule accepts a hydrogen bond from a carbamate nitrogen atom of the neighboring ammonium carbamate chain in the *ab* plane (N...O distance of 2.939 Å), resulting in a channel of H₂O molecules between adjacent ammonium carbamate chains (Figure S95). A CO₂ adsorption energy of -88 kJ/mol was calculated for coadsorption of 1 CO₂ and 1 H₂O per diamine, indicating that water increases the magnitude of the CO₂ binding energy by an estimated 18 kJ/mol compared to CO₂ insertion under dry conditions

(binding energy of -70 kJ/mol). This value is smaller than the 31 ± 2 kJ/mol increase in $-\Delta h_{\text{ads}}$ calculated from the humid vs dry pure CO₂ adsorption isobars, but a comparison of the absolute values may be complicated by nonequilibrium effects in the isobars and the inability to determine the precise composition of the adsorbed phase. Notably, the DFT-calculated binding energy of CO₂ is larger than that of water in the coadsorbed structure, suggesting that the endothermic penalty to desorb H₂O is smaller, and thus H₂O is likely to desorb first. This result is consistent with the minimal differences in the dry and humid CO₂ desorption temperatures observed in mixed-gas isobars (Figure 3). We note that the calculated and experimental NMR shifts for 2-ampd-Mg₂(dobpdc) exposed to dry and humid CO₂ also agree well with the experimental values (Table S20).

Taken together, the humid isobars, breakthrough measurements, spectroscopic data, and vdW-corrected DFT calculations support an increase in the favorability of CO₂ insertion under humid conditions, as a result of an enhancement of the ammonium carbamate chain formation mechanism in the presence of water. In humid breakthrough experiments, the resulting effective decrease in the isothermal CO₂ adsorption step pressure alters the propagation of the adsorption front through the bed. In particular, the single “shock” in the humid CO₂ breakthrough profile suggests that water reduces the effective step pressure and/or alters the shape of the CO₂ adsorption profile at low partial pressures, leading to more favorable performance under humid conditions (Figure S53).

Thermal, Oxidative, and Cycling Stability. Beyond the thermodynamics and kinetics of adsorption, the long-term stability of an adsorbent is a critical consideration for ultimate industrial applications. In particular, the high oxygen content of the NGCC flue gas stream ($\sim 12\%$) is well-known to lead to oxidative degradation of aqueous amine solutions.^{24–27} To

924 evaluate the oxidative stability of 2-ampd-Mg₂(dobpdc), the
 925 material was exposed to a flow of dry air (~21% O₂ in N₂) at
 926 100 °C and atmospheric pressure for 5 h, and the dry, pure
 927 CO₂ isobars were compared before and after exposure.
 928 Minimal changes were observed in the CO₂ adsorption profile
 929 or capacity after this extensive O₂ treatment (Figure 8). In

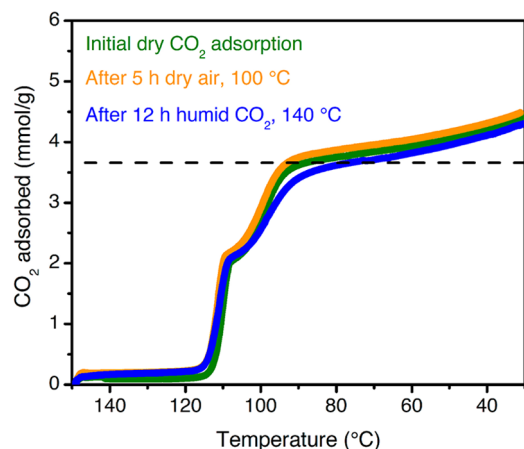


Figure 8. Dry, pure CO₂ adsorption isobars for 2-ampd-Mg₂(dobpdc) as synthesized (green curve), after exposure to a flow of dry air (~21% O₂ in N₂) at 100 °C for 5 h (orange curve), and after exposure to a flow of humid CO₂ at 140 °C for 12 h (blue curve). A ramp rate of 1 °C/min was used in all cases. The dashed black line indicates the theoretical capacity for adsorption of 1 CO₂ per diamine.

930 contrast, dry, oxygen-containing streams at 100 °C have been
 931 found to cause significant degradation of silicas functionalized
 932 with secondary amines.¹¹⁷ In addition, no diamine oxidation
 933 products were detected by IR or by ¹H NMR spectroscopy
 934 after digestion of the O₂-treated material (Figure S72). The
 935 oxidative resistance of 2-ampd-Mg₂(dobpdc) is likely due in
 936 part to the fixed, wide spacing of diamines at metal sites ~7 Å
 937 apart along the channel direction, which serves to mitigate
 938 bimolecular (2 amine molecules) oxidation pathways observed
 939 in other materials.¹¹⁷

940 Adsorbents for carbon capture from NGCC flue gas must
 941 also withstand repeated thermal cycling under humid
 942 conditions. As part of this work, we found that the stability
 943 of diamine-appended variants of Mg₂(dobpdc) and related
 944 materials can be rapidly assessed by exposing the adsorbent to
 945 a flow of humid CO₂ for 12 h at the relevant desorption
 946 temperature (here, 140 °C) in a thermogravimetric analyzer,
 947 simulating hundreds of adsorption/desorption cycles (SI
 948 Section S16). The humid CO₂ adsorption capacities before
 949 and after such accelerated decomposition experiments can be
 950 compared to evaluate any capacity loss, and the material can be
 951 digested after the test to detect diamine volatilization or
 952 degradation. Notably, after treatment with flowing humid CO₂
 953 at 140 °C for 12 h, 2-ampd-Mg₂(dobpdc) retains its step-
 954 shaped adsorption profile (Figure 8, blue curve) with only a
 955 slight capacity loss at 40 °C (original: 4.20 mmol/g; after
 956 humid CO₂ treatment: 4.11 mmol/g). In addition, almost no
 957 diamine volatilization (~2%) from the framework was
 958 observed. We further tested the stability of 2-ampd-
 959 Mg₂(dobpdc) to accelerated decomposition experiments at
 960 higher temperatures, representative of a potential process
 961 failure. At temperatures as high as 180 °C, 2-ampd-

Mg₂(dobpdc) retains more than 90% of its adsorption capacity 962
 (Table S15), and the material remains highly crystalline even 963
 after treatment with a humid CO₂ stream at 220 °C for 12 h 964
 (Figure S70). Evaluation of a number of promising diamine- 965
 appended variants of Mg₂(dobpdc) for CO₂ capture from 966
 NGCC flue gas further revealed that the thermal stability of 2- 967
 ampd-Mg₂(dobpdc) is nearly unparalleled among this family 968
 of materials (Table S14). In addition, the stability of 2-ampd- 969
 Mg₂(dobpdc) is far superior to that of the representative 970
 amine-functionalized silica MCM-41-PEI-50, which undergoes 971
 urea formation and significant capacity loss (~17%) at 40 °C 972
 following exposure to humid CO₂ for 12 h at 140 °C (Figures 973
 S75–S77). The exceptional stability of 2-ampd-Mg₂(dobpdc) 974
 to humid gas streams at high temperatures makes it particularly 975
 promising for long-term application in a CO₂ capture process. 976

The stability of 2-ampd-Mg₂(dobpdc) in a TSA process 977
 was further evaluated by performing 750 adsorption (humid 978
 4% CO₂ in N₂, 40 °C) and desorption (humid CO₂, 140 °C) 979
 cycles using a thermogravimetric analyzer (Figure 9, see SI 980 99

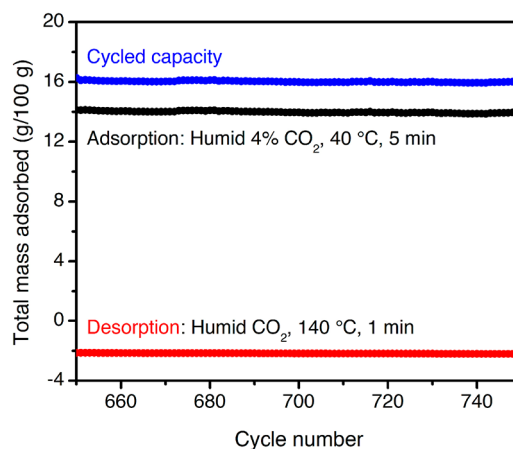


Figure 9. Cycling data for the final 100 of 750 adsorption/desorption cycles for 2-ampd-Mg₂(dobpdc) in a simulated temperature swing adsorption process. Adsorption: humid 4% CO₂ in N₂, 40 °C, 5 min (black, cycle maxima). Desorption: Humid CO₂, 140 °C, 1 min (red, cycle minima). The cycled capacity (difference) is shown in blue. The baseline value of 0 g/100 g is defined as the mass after activation under 4% CO₂ in N₂ at 150 °C for 20 min prior to the first cycle. The diamine loading was reduced from 100% to 94% after this experiment. The same final loading was observed after 200 adsorption/desorption cycles, suggesting that the diamine loading stabilizes after initial loss. The weight loss due to diamine volatilization correlates with equilibration of the mass upon desorption to the observed negative baseline value.

Figure S80 for the full cycling data). Consistent with the 981
 accelerated decomposition test results (Figure 8), 2-ampd- 982
 Mg₂(dobpdc) exhibited a stable cycling capacity under humid 983
 simulated NGCC flue gas (Figure 9). The same final diamine 984
 loading (~94%) was observed after both 200 and 750 cycles, 985
 suggesting that the loading stabilizes after a small amount of 986
 initial diamine volatilization, likely from weakly bound defect 987
 or surface sites. Notably, a high CO₂/H₂O cycling capacity of 988
 16.0 g/100 g was observed for the 750th cycle, comparable to 989
 the adsorption capacity from a dry 4% CO₂ in N₂ stream at 40 990
 °C (15.8 g/100 g). Nearly the same cycled capacity (15.3 g/ 991
 100 g) could also be achieved over 200 tested cycles with a 992
 higher adsorption temperature of 60 °C (Figure S81). Short 993
 adsorption (5 min) and desorption (1 min) times were used in 994

these experiments, indicating rapid kinetics despite the low CO₂ content of the simulated flue gas stream. Overall, the exceptional stability of 2-ampd–Mg₂(dobpdc) and excellent performance in breakthrough and cycling experiments support further development of this promising adsorbent for CO₂ capture from the emissions of gas-fired power plants.

CONCLUSIONS

Natural gas offers significant environmental advantages as an alternative to coal by enabling approximately 50% lower CO₂ emissions per unit of electricity produced. Capturing and sequestering the CO₂ emissions from gas-fired power plants provides an attractive option to achieve even greater emission reductions. We have shown that the metal–organic framework 2-ampd–Mg₂(dobpdc) is a promising candidate for post-combustion CO₂ capture from the emissions of NGCC power stations. In particular, as a result of the constituent cyclic diamine, this material overcomes the trade-off between stability and capacity encountered with related cooperative adsorbents featuring linear 1°/2° diamines. Importantly, in breakthrough experiments simulating a fixed-bed adsorption process, 2-ampd–Mg₂(dobpdc) exhibits single-shock breakthrough profiles under humid conditions, in contrast to the multimodal elution profiles observed under dry conditions. This advantageous result is attributed to stabilizing H₂O–carbamate interactions, a conclusion supported by mixed-gas adsorption experiments, spectroscopic characterization, and vdW-corrected DFT calculations. Finally, 2-ampd–Mg₂(dobpdc) achieves the challenging practical criteria required of a material for CCS from NGCC emissions, namely a high CO₂ swing capacity as well as high thermal, oxidative, and cycling stability. Continued development of 2-ampd–Mg₂(dobpdc) at larger scales and in structured forms will enable modeling of heat and mass transfer and support bench-scale testing.

More broadly, this report achieves key advances toward the deployment of cooperative adsorbents in industrial CO₂ separations. First, we have reiterated the importance of considering CO₂ “slip” in adsorbent and process design for CO₂ capture applications with dry mixtures.^{45,84} Second, and most importantly, we have established that presaturating the adsorbent bed with water can significantly enhance the CO₂ capture performance of diamine-appended, cooperative adsorbents by mitigating or eliminating CO₂ slip. Third, we have shown that experiments under flow conditions (such as isobars collected with slow temperature ramp rates under varying CO₂ concentrations) may predict the performance of cooperative adsorbents more accurately than single-component, volumetric adsorption isotherms. Finally, we have shown that TSA processes with cooperative adsorbents can utilize higher adsorption temperatures (here, 60 °C or higher instead of 40 °C) that could serve to mitigate water coadsorption and reduce operating costs related to cooling the flue gas stream. Moving forward, we expect that these discoveries will be of value in the design of cooperative adsorbents for other challenging CO₂ capture processes, such as the direct capture of CO₂ from air.

Full characterization of all adsorbents and additional experimental details (PDF)
Crystallographic data for Zn₂(dobpdc)(2-ampd)_{1.76}(C₇H₈)_{0.79} (CIF)
Crystallographic data for 2-ampd–CO₂ (CIF)
DFT-calculated structure of Mg₂(dobpdc)(2-ampd)₂ (CIF)
DFT-calculated structure of Mg₂(dobpdc)(2-ampd–CO₂)₂ (CIF)
DFT-calculated structure of Mg₂(dobpdc)(2-ampd)₂(H₂O)₂ (CIF)
DFT-calculated structure of Mg₂(dobpdc)(2-ampd–CO₂)₂(H₂O)₂ (CIF)
DFT-calculated structure of cocaine (CIF)
DFT-calculated structure of glycine (CIF)

AUTHOR INFORMATION

Corresponding Author

*jrlong@berkeley.edu

ORCID

Phillip J. Milner: 0000-0002-2618-013X

Alexander C. Forse: 0000-0001-9592-9821

Jeffrey A. Reimer: 0000-0002-4191-3725

Simon C. Weston: 0000-0002-7439-5055

Jeffrey R. Long: 0000-0002-5324-1321

Present Address

◆Department of Chemistry and Chemical Biology, Cornell University, Ithaca, New York, 14853, United States.

Author Contributions

¶These authors contributed equally to this work.

Notes

The authors declare the following competing financial interest(s): J.R.L. has a financial interest in Mosaic Materials, Inc., a start-up company working to commercialize metal-organic frameworks for gas separations. The University of California, Berkeley and ExxonMobil Research and Engineering Company have applied for a patent on some of the materials discussed herein, on which P.J.M., R.L.S., S.C.W., and J.R.L. are included as inventors.

ACKNOWLEDGMENTS

We gratefully acknowledge ExxonMobil Research and Engineering Company for financial support of this work. We thank the National Institute of General Medical Sciences of the National Institutes of Health for a postdoctoral fellowship for P.J.M. (F32GM120799). The content is solely the responsibility of the authors and does not necessarily represent the official views of the National Institutes of Health. We thank the Philomathia Foundation and Berkeley Energy and Climate Institute for support of A.C.F. through a postdoctoral fellowship. Work at the Molecular Foundry was supported by the Office of Science, Office of Basic Energy Sciences, U.S. Department of Energy, under Contract DE-AC02-05CH11231, and computational resources were provided by the Department of Energy (LBNL Lawrence Livermore and NERSC). This research also used the Savio computational cluster resource provided by the Berkeley Research Computing program at the University of California, Berkeley (supported by the UC Berkeley Chancellor, Vice Chancellor for Research, and Chief Information Officer). Single-crystal X-ray diffraction data were collected on Beamline 12.2.1 at the Advanced Light

Source at Lawrence Berkeley National Laboratory, which is supported by the Director, Office of Science, Office of Basic Energy Sciences, of the U.S. Department of Energy under Contract No. DE-AC02-05CH11231. Synchrotron powder X-ray diffraction data were collected at the Advanced Photon Source, a U.S. Department of Energy Office of Science User Facility operated for the DOE Office of Science by Argonne National Laboratory under Contract No. DE-AC02-06CH11357. We thank Dr. Joseph Falkowski (ExxonMobil Research and Engineering Company), Dr. Miguel Gonzalez (UC Berkeley), and Dr. Jeffrey Martell (UC Berkeley) for helpful discussions; Eugene Kim (UC Berkeley) and Julia Oktawiec (UC Berkeley) for experimental assistance; and Dr. Katie Meihaus (UC Berkeley) for editorial assistance.

REFERENCES

- (1) *CO₂ Emissions from Fuel Combustion 2017—Highlights*; International Energy Agency: Paris, France, 2017.
- (2) Pachauri, R. K.; Allen, M. R.; Barros, V. R.; Broome, J.; Cramer, W.; Christ, R.; Church, J. A.; Clarke, L.; Dahe, Q.; Dasgupta, P. *Climate Change 2014: Synthesis Report. Contribution of Working Groups I, II and III to the Fifth Assessment Report of the Intergovernmental Panel on Climate Change*; IPCC, 2014.
- (3) Chu, S. Carbon Capture and Sequestration. *Science* **2009**, *325* (5948), 1599–1599.
- (4) Bui, M.; Adjiman, C. S.; Bardow, A.; Anthony, E. J.; Boston, A.; Brown, S.; Fennell, P. S.; Fuss, S.; Galindo, A.; Hackett, L. A.; Hallett, J. P.; Herzog, H. J.; Jackson, G.; Kemper, J.; Krevor, S.; Maitland, G. C.; Matuszewski, M.; Metcalfe, I. S.; Petit, C.; Puxty, G.; Reimer, J.; Reiner, D. M.; Rubin, E. S.; Scott, S. A.; Shah, N.; Smit, B.; Trusler, J. P. M.; Webley, P.; Wilcox, J.; Mac Dowell, N. Carbon Capture and Storage (CCS): The Way Forward. *Energy Environ. Sci.* **2018**, *11*, 1062–1076.
- (5) Stauffer, P. H.; Keating, G. N.; Middleton, R. S.; Viswanathan, H. S.; Berchtold, K. A.; Singh, R. P.; Pawar, R. J.; Mancino, A. Greening Coal: Breakthroughs and Challenges in Carbon Capture and Storage. *Environ. Sci. Technol.* **2011**, *45* (20), 8597–8604.
- (6) *World Energy Outlook 2017*; International Energy Agency, 2017. DOI: 10.1787/weo-2017-en.
- (7) *Annual Energy Outlook 2018 with Projections to 2050*; U.S. Energy Information Administration, 2018.
- (8) *CO₂ Capture at Gas Fired Power Plants*; IEAGHG, 2012.
- (9) *Carbon Dioxide Capture for Natural Gas and Industrial Applications*; Quadrennial Technology Review 2015; U.S. Department of Energy, 2015.
- (10) *Carbon Capture Opportunities for Natural Gas Fired Power Systems*; U.S. Department of Energy, 2017.
- (11) *Cost and Performance Baseline for Fossil Energy Plants. Vol. 1a: Bituminous Coal (PC) and Natural Gas to Electricity*, Revision 3; DOE/NETL-2015/1723; U.S. Department of Energy, National Energy Technology Laboratory, 2015.
- (12) Khatri, R. A.; Chuang, S. S. C.; Soong, Y.; Gray, M. Thermal and Chemical Stability of Regenerable Solid Amine Sorbent for CO₂ Capture. *Energy Fuels* **2006**, *20* (4), 1514–1520.
- (13) Uyanga, I. J.; Idem, R. O. Studies of SO₂- and O₂-Induced Degradation of Aqueous MEA during CO₂ Capture from Power Plant Flue Gas Streams. *Ind. Eng. Chem. Res.* **2007**, *46* (8), 2558–2566.
- (14) Belmabkhout, Y.; Sayari, A. Isothermal versus Non-Isothermal Adsorption-Desorption Cycling of Triamine-Grafted Pore-Expanded MCM-41 Mesoporous Silica for CO₂ Capture from Flue Gas. *Energy Fuels* **2010**, *24* (9), 5273–5280.
- (15) Sjostrom, S.; Krutka, H. Evaluation of Solid Sorbents as a Retrofit Technology for CO₂ Capture. *Fuel* **2010**, *89* (6), 1298–1306.
- (16) Han, S.; Huang, Y.; Watanabe, T.; Dai, Y.; Walton, K. S.; Nair, S.; Sholl, D. S.; Meredith, J. C. High-Throughput Screening of Metal–Organic Frameworks for CO₂ Separation. *ACS Comb. Sci.* **2012**, *14* (4), 263–267.
- (17) Yu, K.; Kiesling, K.; Schmidt, J. R. Trace Flue Gas Contaminants Poison Coordinatively Unsaturated Metal–Organic Frameworks: Implications for CO₂ Adsorption and Separation. *J. Phys. Chem. C* **2012**, *116* (38), 20480–20488.
- (18) Hallenbeck, A. P.; Kitchin, J. R. Effects of O₂ and SO₂ on the Capture Capacity of a Primary-Amine Based Polymeric CO₂ Sorbent. *Ind. Eng. Chem. Res.* **2013**, *52* (31), 10788–10794.
- (19) Rezaei, F.; Jones, C. W. Stability of Supported Amine Adsorbents to SO₂ and NO_x in Postcombustion CO₂ Capture. 1. Single-Component Adsorption. *Ind. Eng. Chem. Res.* **2013**, *52* (34), 12192–12201.
- (20) Berger, A. H.; Bhowan, A. S. Selection of Optimal Solid Sorbents for CO₂ Capture Based on Gas Phase CO₂ Composition. *Energy Procedia* **2014**, *63*, 2092–2099.
- (21) Rezaei, F.; Grahn, M. Thermal Management of Structured Adsorbents in CO₂ Capture Processes. *Ind. Eng. Chem. Res.* **2012**, *51* (10), 4025–4034.
- (22) Rochelle, G. T. Amine Scrubbing for CO₂ Capture. *Science* **2009**, *325* (5948), 1652–1654.
- (23) Bhowan, A. S.; Freeman, B. C. Analysis and Status of Post-Combustion Carbon Dioxide Capture Technologies. *Environ. Sci. Technol.* **2011**, *45* (20), 8624–8632.
- (24) Gouedard, C.; Picq, D.; Launay, F.; Carrette, P.-L. Amine Degradation in CO₂ Capture. I. A Review. *Int. J. Greenhouse Gas Control* **2012**, *10*, 244–270.
- (25) Fredriksen, S. B.; Jens, K.-J. Oxidative Degradation of Aqueous Amine Solutions of MEA, AMP, MDEA, Pz: A Review. *Energy Procedia* **2013**, *37*, 1770–1777.
- (26) Vega, F.; Sanna, A.; Navarrete, B.; Maroto-Valer, M. M.; Cortés, V. J. Degradation of Amine-based Solvents in CO₂ Capture Process by Chemical Absorption. *Greenhouse Gases: Sci. Technol.* **2014**, *4* (6), 707–733.
- (27) Mazari, S. A.; Si Ali, B.; Jan, B. M.; Saeed, I. M.; Nizamuddin, S. An Overview of Solvent Management and Emissions of Amine-Based CO₂ Capture Technology. *Int. J. Greenhouse Gas Control* **2015**, *34*, 129–140.
- (28) Choi, S.; Drese, J. H.; Jones, C. W. Adsorbent Materials for Carbon Dioxide Capture from Large Anthropogenic Point Sources. *ChemSusChem* **2009**, *2* (9), 796–854.
- (29) Bae, Y.-S.; Snurr, R. Q. Development and Evaluation of Porous Materials for Carbon Dioxide Separation and Capture. *Angew. Chem., Int. Ed.* **2011**, *50* (49), 11586–11596.
- (30) Bollini, P.; Didas, S. A.; Jones, C. W. Amine-Oxide Hybrid Materials for Acid Gas Separations. *J. Mater. Chem.* **2011**, *21* (39), 15100–15120.
- (31) Li, J.-R.; Ma, Y.; McCarthy, M. C.; Sculley, J.; Yu, J.; Jeong, H.-K.; Balbuena, P. B.; Zhou, H.-C. Carbon Dioxide Capture-Related Gas Adsorption and Separation in Metal–Organic Frameworks. *Coord. Chem. Rev.* **2011**, *255* (15–16), 1791–1823.
- (32) Wang, Q.; Luo, J.; Zhong, Z.; Borgna, A. CO₂ Capture by Solid Adsorbents and Their Applications: Current Status and New Trends. *Energy Environ. Sci.* **2011**, *4* (1), 42–55.
- (33) Liu, J.; Thallapally, P. K.; McGrail, B. P.; Brown, D. R.; Liu, J. Progress in Adsorption-Based CO₂ Capture by Metal–Organic Frameworks. *Chem. Soc. Rev.* **2012**, *41* (6), 2308–2322.
- (34) Samanta, A.; Zhao, A.; Shimizu, G. K. H.; Sarkar, P.; Gupta, R. Post-Combustion CO₂ Capture Using Solid Sorbents: A Review. *Ind. Eng. Chem. Res.* **2012**, *51* (4), 1438–1463.
- (35) Sumida, K.; Rogow, D. L.; Mason, J. A.; McDonald, T. M.; Bloch, E. D.; Herm, Z. R.; Bae, T.-H.; Long, J. R. Carbon Dioxide Capture in Metal–Organic Frameworks. *Chem. Rev.* **2012**, *112* (2), 724–781.
- (36) Huck, J. M.; Lin, L.-C.; Berger, A. H.; Shahrak, M. N.; Martin, R. L.; Bhowan, A. S.; Haranczyk, M.; Reuter, K.; Smit, B. Evaluating Different Classes of Porous Materials for Carbon Capture. *Energy Environ. Sci.* **2014**, *7* (12), 4132–4146.
- (37) Webley, P. A. Adsorption Technology for CO₂ Separation and Capture: A Perspective. *Adsorption* **2014**, *20* (2–3), 225–231.

- (38) Lee, S.-Y.; Park, S.-J. A Review on Solid Adsorbents for Carbon Dioxide Capture. *J. Ind. Eng. Chem.* **2015**, *23*, 1–11.
- (39) Sanz-Pérez, E. S.; Murdock, C. R.; Didas, S. A.; Jones, C. W. Direct Capture of CO₂ from Ambient Air. *Chem. Rev.* **2016**, *116* (19), 11840–11876.
- (40) Unveren, E. E.; Monkul, B. O.; Sartoglan, S.; Karademir, N.; Alper, E. Solid Amine Sorbents for CO₂ Capture by Chemical Adsorption: A Review. *Petroleum* **2017**, *3* (1), 37–50.
- (41) Siegelman, R. L.; Milner, P. J.; Kim, E. J.; Weston, S. C.; Long, J. R. Challenges and Opportunities for Adsorption-Based CO₂ Capture from Natural Gas Combined Cycle Emissions. *Energy Environ. Sci.* **2019**, *12* (7), 2161–2173.
- (42) Xu, X.; Song, C.; Miller, B. G.; Scaroni, A. W. Adsorption Separation of Carbon Dioxide from Flue Gas of Natural Gas-Fired Boiler by a Novel Nanoporous “Molecular Basket” Adsorbent. *Fuel Process. Technol.* **2005**, *86* (14), 1457–1472.
- (43) Grande, C. A.; Ribeiro, R. P. P. L.; Rodrigues, A. E. CO₂ Capture from NGCC Power Stations Using Electric Swing Adsorption (ESA). *Energy Fuels* **2009**, *23* (5), 2797–2803.
- (44) Seif El Nasr, A.; Nelson, T.; Kataria, A.; Abu-Zahra, M. R. M. Benchmarking of a Novel Solid Sorbent CO₂ Capture Process for NGCC Power Generation. *Int. J. Greenhouse Gas Control* **2015**, *42*, 583–592.
- (45) Hefti, M.; Joss, L.; Bjelobrk, Z.; Mazzotti, M. On the Potential of Phase-Change Adsorbents for CO₂ Capture by Temperature Swing Adsorption. *Faraday Discuss.* **2016**, *192*, 153–179.
- (46) Gibson, J. A. A.; Mangano, E.; Shiko, E.; Greenaway, A. G.; Gromov, A. V.; Lozinska, M. M.; Friedrich, D.; Campbell, E. E. B.; Wright, P. A.; Brandani, S. Adsorption Materials and Processes for Carbon Capture from Gas-Fired Power Plants: AMPGas. *Ind. Eng. Chem. Res.* **2016**, *55* (13), 3840–3851.
- (47) Zhang, W.; Sun, C.; Snape, C. E.; Irons, R.; Stebbing, S.; Alderson, T.; Fitzgerald, D.; Liu, H. Process Simulations of Post-Combustion CO₂ Capture for Coal and Natural Gas-Fired Power Plants Using a Polyethyleneimine/Silica Adsorbent. *Int. J. Greenhouse Gas Control* **2017**, *58*, 276–289.
- (48) Dijkstra, J. W.; Walspurger, S.; Elzinga, G. D.; Pieterse, J. A. Z.; Boon, J.; Haije, W. G. Evaluation of Postcombustion CO₂ Capture by a Solid Sorbent with Process Modeling Using Experimental CO₂ and H₂O Adsorption Characteristics. *Ind. Eng. Chem. Res.* **2018**, *57* (4), 1245–1261.
- (49) McDonald, T. M.; Lee, W. R.; Mason, J. A.; Wiers, B. M.; Hong, C. S.; Long, J. R. Capture of Carbon Dioxide from Air and Flue Gas in the Alkylamine-Appended Metal–Organic Framework mmen-Mg₂(dobpdc). *J. Am. Chem. Soc.* **2012**, *134* (16), 7056–7065.
- (50) McDonald, T. M.; Mason, J. A.; Kong, X.; Bloch, E. D.; Gygi, D.; Dani, A.; Crocellà, V.; Giordanino, F.; Odoh, S. O.; Drisdell, W. S.; Vlasisavljevič, B.; Dzubak, A. L.; Poloni, R.; Schnell, S. K.; Planas, N.; Lee, K.; Pascal, T.; Wan, L. F.; Prendergast, D.; Neaton, J. B.; Smit, B.; Kortright, J. B.; Gagliardi, L.; Bordiga, S.; Reimer, J. A.; Long, J. R. Cooperative Insertion of CO₂ in Diamine-Appended Metal–Organic Frameworks. *Nature* **2015**, *519* (7543), 303–308.
- (51) Siegelman, R. L.; McDonald, T. M.; Gonzalez, M. I.; Martell, J. D.; Milner, P. J.; Mason, J. A.; Berger, A. H.; Bhowan, A. S.; Long, J. R. Controlling Cooperative CO₂ Adsorption in Diamine-Appended Mg₂(dobpdc) Metal–Organic Frameworks. *J. Am. Chem. Soc.* **2017**, *139* (30), 10526–10538.
- (52) Milner, P. J.; Siegelman, R. L.; Forse, A. C.; Gonzalez, M. I.; Runčevski, T.; Martell, J. D.; Reimer, J. A.; Long, J. R. A Diaminopropane-Appended Metal–Organic Framework Enabling Efficient CO₂ Capture from Coal Flue Gas via a Mixed Adsorption Mechanism. *J. Am. Chem. Soc.* **2017**, *139* (38), 13541–13553.
- (53) Milner, P. J.; Martell, J. D.; Siegelman, R. L.; Gygi, D.; Weston, S. C.; Long, J. R. Overcoming Double-Step CO₂ Adsorption and Minimizing Water Co-Adsorption in Bulky Diamine-Appended Variants of Mg₂(dobpdc). *Chem. Sci.* **2018**, *9* (1), 160–174.
- (54) Lee, W. R.; Hwang, S. Y.; Ryu, D. W.; Lim, K. S.; Han, S. S.; Moon, D.; Choi, J.; Hong, C. S. Diamine-Functionalized Metal–Organic Framework: Exceptionally High CO₂ Capacities from Ambient Air and Flue Gas, Ultrafast CO₂ Uptake Rate, and Adsorption Mechanism. *Energy Environ. Sci.* **2014**, *7* (2), 744–751.
- (55) Lee, W. R.; Jo, H.; Yang, L.-M.; Lee, H.; Ryu, D. W.; Lim, K. S.; Song, J. H.; Min, D. Y.; Han, S. S.; Seo, J. G.; Park, Y. K.; Moon, D.; Hong, C. S. Exceptional CO₂ Working Capacity in a Heterodiamine-Grafted Metal–Organic Framework. *Chem. Sci.* **2015**, *6* (7), 3697–3705.
- (56) Jo, H.; Lee, W. R.; Kim, N. W.; Jung, H.; Lim, K. S.; Kim, J. E.; Kang, D. W.; Lee, H.; Hiremath, V.; Seo, J. G.; Jin, H.; Moon, D.; Han, S. S.; Hong, C. S. Fine-Tuning of the Carbon Dioxide Capture Capability of Diamine-Grafted Metal–Organic Framework Adsorbents Through Amine Functionalization. *ChemSusChem* **2017**, *10* (3), 541–550.
- (57) Lee, W. R.; Kim, J. E.; Lee, S. J.; Kang, M.; Kang, D. W.; Lee, H. Y.; Hiremath, V.; Seo, J. G.; Jin, H.; Moon, D.; Cho, M.; Jung, Y.; Hong, C. S. Diamine-Functionalization of a Metal–Organic Framework Adsorbent for Superb Carbon Dioxide Adsorption and Desorption Properties. *ChemSusChem* **2018**, *11* (10), 1694–1707.
- (58) Kang, M.; Kim, J. E.; Kang, D. W.; Lee, H. Y.; Moon, D.; Hong, C. S. A Diamine-Grafted Metal–Organic Framework with Outstanding CO₂ Capture Properties and a Facile Coating Approach for Imparting Exceptional Moisture Stability. *J. Mater. Chem. A* **2019**, *7* (14), 8177–8183.
- (59) Hong, C. S.; Kang, M.; Kang, D. W. Post-Synthetic Diamine-Functionalization of MOF-74 Type Frameworks for Effective Carbon Dioxide Separation. *Dalton Trans* **2019**, *48*, 2263–2270.
- (60) Mosaic Materials, Inc., <http://mosaicmaterials.com/>.
- (61) Forse, A. C.; Milner, P. J.; Lee, J.-H.; Redfearn, H. N.; Oktawiec, J.; Siegelman, R. L.; Martell, J. D.; Dinakar, B.; Porter-Zasada, L. B.; Gonzalez, M. I.; Neaton, J. B.; Long, J. R.; Reimer, J. A. Elucidating CO₂ Chemisorption in Diamine-Appended Metal–Organic Frameworks. *J. Am. Chem. Soc.* **2018**, *140* (51), 18016–18031.
- (62) NIST WebBook, <https://webbook.nist.gov/>.
- (63) Campbell, C. T.; Sellers, J. R. V. Enthalpies and Entropies of Adsorption on Well-Defined Oxide Surfaces: Experimental Measurements. *Chem. Rev.* **2013**, *113* (6), 4106–4135.
- (64) Bertani, P.; Raya, J.; Bechinger, B. ¹⁵N Chemical Shift Referencing in Solid State NMR. *Solid State Nucl. Magn. Reson.* **2014**, *61–62*, 15–18.
- (65) Blöchl, P. E. Projector Augmented-Wave Method. *Phys. Rev. B: Condens. Matter Mater. Phys.* **1994**, *50* (24), 17953–17979.
- (66) Kresse, G.; Joubert, D. From Ultrasoft Pseudopotentials to the Projector Augmented-Wave Method. *Phys. Rev. B: Condens. Matter Mater. Phys.* **1999**, *59* (3), 1758–1775.
- (67) Kresse, G.; Hafner, J. Ab Initio Molecular Dynamics for Liquid Metals. *Phys. Rev. B: Condens. Matter Mater. Phys.* **1993**, *47* (1), 558–561.
- (68) Kresse, G.; Hafner, J. Ab Initio Molecular-Dynamics Simulation of the Liquid-Metal–Amorphous-Semiconductor Transition in Germanium. *Phys. Rev. B: Condens. Matter Mater. Phys.* **1994**, *49* (20), 14251–14269.
- (69) Kresse, G.; Furthmüller, J. Efficient Iterative Schemes for Ab Initio Total-Energy Calculations Using a Plane-Wave Basis Set. *Phys. Rev. B: Condens. Matter Mater. Phys.* **1996**, *54* (16), 11169–11186.
- (70) Kresse, G.; Furthmüller, J. Efficiency of Ab-Initio Total Energy Calculations for Metals and Semiconductors Using a Plane-Wave Basis Set. *Comput. Mater. Sci.* **1996**, *6* (1), 15–50.
- (71) Lee, K.; Murray, E. D.; Kong, L.; Lundqvist, B. I.; Langreth, D. C. Higher-Accuracy van Der Waals Density Functional. *Phys. Rev. B: Condens. Matter Mater. Phys.* **2010**, *82* (8), 081101.
- (72) Elsässer, C.; Fahnle, M.; Chan, C. T.; Ho, K. M. Density-Functional Energies and Forces with Gaussian-Broadened Fractional Occupations. *Phys. Rev. B: Condens. Matter Mater. Phys.* **1994**, *49* (19), 13975–13978.
- (73) Baiaes, M.; Widdifield, C. M.; Dumez, J.-N.; Thompson, H. P. G.; Cooper, T. G.; Salager, E.; Bassil, S.; Stein, R. S.; Lesage, A.; Day, G. M.; Emsley, L. Powder Crystallography of Pharmaceutical Materials by Combined Crystal Structure Prediction and Solid-State

- ¹H NMR Spectroscopy. *Phys. Chem. Chem. Phys.* **2013**, *15* (21), 8069–8080.
- (74) Ali, U.; Agbonghae, E. O.; Hughes, K. J.; Ingham, D. B.; Ma, L.; Pourkashanian, M. Techno-Economic Process Design of a Commercial-Scale Amine-Based CO₂ Capture System for Natural Gas Combined Cycle Power Plant with Exhaust Gas Recirculation. *Appl. Therm. Eng.* **2016**, *103*, 747–758.
- (75) Zhang, Z.; Yao, Z.-Z.; Xiang, S.; Chen, B. Perspective of Microporous Metal–Organic Frameworks for CO₂ Capture and Separation. *Energy Environ. Sci.* **2014**, *7* (9), 2868.
- (76) Sabouni, R.; Kazemian, H.; Rohani, S. Carbon Dioxide Capturing Technologies: A Review Focusing on Metal Organic Framework Materials (MOFs). *Environ. Sci. Pollut. Res.* **2014**, *21* (8), 5427–5449.
- (77) Wang, Q.; Bai, J.; Lu, Z.; Pan, Y.; You, X. Finely Tuning MOFs towards High-Performance Post-Combustion CO₂ Capture Materials. *Chem. Commun.* **2016**, *52* (3), 443–452.
- (78) Yu, J.; Xie, L.-H.; Li, J.-R.; Ma, Y.; Seminario, J. M.; Balbuena, P. B. CO₂ Capture and Separations Using MOFs: Computational and Experimental Studies. *Chem. Rev.* **2017**, *117* (14), 9674–9754.
- (79) Alkhabbaz, M. A.; Bollini, P.; Foo, G. S.; Sievers, C.; Jones, C. W. Important Roles of Enthalpic and Entropic Contributions to CO₂ Capture from Simulated Flue Gas and Ambient Air Using Mesoporous Silica Grafted Amines. *J. Am. Chem. Soc.* **2014**, *136* (38), 13170–13173.
- (80) Xu, X.; Song, C.; Andresen, J. M.; Miller, B. G.; Scaroni, A. W. Novel Polyethylenimine-Modified Mesoporous Molecular Sieve of MCM-41 Type as High-Capacity Adsorbent for CO₂ Capture. *Energy Fuels* **2002**, *16* (6), 1463–1469.
- (81) Mason, J. A.; McDonald, T. M.; Bae, T.-H.; Bachman, J. E.; Sumida, K.; Dutton, J. J.; Kaye, S. S.; Long, J. R. Application of a High-Throughput Analyzer in Evaluating Solid Adsorbents for Post-Combustion Carbon Capture via Multicomponent Adsorption of CO₂, N₂, and H₂O. *J. Am. Chem. Soc.* **2015**, *137* (14), 4787–4803.
- (82) Liao, P.-Q.; Chen, X.-W.; Liu, S.-Y.; Li, X.-Y.; Xu, Y.-T.; Tang, R.; Rui, Z.; Ji, H.; Zhang, J.-P.; Chen, X.-M. Putting an Ultrahigh Concentration of Amine Groups into a Metal–Organic Framework for CO₂ Capture at Low Pressures. *Chem. Sci.* **2016**, *7* (10), 6528–6533.
- (83) Bien, C. E.; Chen, K. K.; Chien, S.-C.; Reiner, B. R.; Lin, L.-C.; Wade, C. R.; Ho, W. S. W. Bioinspired Metal–Organic Framework for Trace CO₂ Capture. *J. Am. Chem. Soc.* **2018**, *140* (40), 12662–12666.
- (84) Darunte, L.; Sen, T.; Bhawanani, C.; Walton, K. S.; Sholl, D. S.; Realff, M. J.; Jones, C. W. Moving Beyond Adsorption Capacity in Design of Adsorbents for CO₂ Capture from Ultra-Dilute Feeds: Kinetics of CO₂ Adsorption in Materials with Stepped Isotherms. *Ind. Eng. Chem. Res.* **2019**, *58* (1), 366–377.
- (85) Zhang, W.; Shan, Y.; Seidel-Morgenstern, A. Breakthrough Curves and Elution Profiles of Single Solutes in Case of Adsorption Isotherms with Two Inflection Points. *J. Chromatogr. A* **2006**, *1107* (1–2), 216–225.
- (86) Helfferich, F. G.; Carr, P. W. Non-Linear Waves in Chromatography. *J. Chromatogr. A* **1993**, *629* (2), 97–122.
- (87) Golden, F. M. *Theory of Fixed-Bed Performance for Ion Exchange Accompanied by Chemical Reaction*; Ph.D. Thesis, University of California: Berkeley, CA, 1973.
- (88) Satyapal, S.; Filburn, T.; Trela, J.; Strange, J. Performance and Properties of a Solid Amine Sorbent for Carbon Dioxide Removal in Space Life Support Applications. *Energy Fuels* **2001**, *15* (2), 250–255.
- (89) Huang, H. Y.; Yang, R. T.; Chinn, D.; Munson, C. L. Amine-Grafted MCM-48 and Silica Xerogel as Superior Sorbents for Acidic Gas Removal from Natural Gas. *Ind. Eng. Chem. Res.* **2003**, *42* (12), 2427–2433.
- (90) Xu, X.; Song, C.; Miller, B. G.; Scaroni, A. W. Influence of Moisture on CO₂ Separation from Gas Mixture by a Nanoporous Adsorbent Based on Polyethylenimine-Modified Molecular Sieve MCM-41. *Ind. Eng. Chem. Res.* **2005**, *44* (21), 8113–8119.
- (91) Serna-Guerrero, R.; Belmabkhout, Y.; Sayari, A. Further Investigations of CO₂ Capture Using Triamine-Grafted Pore-Expanded Mesoporous Silica. *Chem. Eng. J.* **2010**, *158* (3), 513–519.
- (92) Serna-Guerrero, R.; Belmabkhout, Y.; Sayari, A. Triamine-Grafted Pore-Expanded Mesoporous Silica for CO₂ Capture: Effect of Moisture and Adsorbent Regeneration Strategies. *Adsorption* **2010**, *16* (6), 567–575.
- (93) Goeppert, A.; Czaun, M.; May, R. B.; Prakash, G. K. S.; Olah, G. A.; Narayanan, S. R. Carbon Dioxide Capture from the Air Using a Polyamine Based Regenerable Solid Adsorbent. *J. Am. Chem. Soc.* **2011**, *133* (50), 20164–20167.
- (94) Fan, Y.; Lively, R. P.; Labreche, Y.; Rezaei, F.; Koros, W. J.; Jones, C. W. Evaluation of CO₂ Adsorption Dynamics of Polymer/Silica Supported Poly(ethylenimine) Hollow Fiber Sorbents in Rapid Temperature Swing Adsorption. *Int. J. Greenhouse Gas Control* **2014**, *21*, 61–71.
- (95) Didas, S. A.; Sakwa-Novak, M. A.; Foo, G. S.; Sievers, C.; Jones, C. W. Effect of Amine Surface Coverage on the Co-Adsorption of CO₂ and Water: Spectral Deconvolution of Adsorbed Species. *J. Phys. Chem. Lett.* **2014**, *5* (23), 4194–4200.
- (96) Hahn, M. W.; Steib, M.; Jentys, A.; Lercher, J. A. Mechanism and Kinetics of CO₂ Adsorption on Surface Bonded Amines. *J. Phys. Chem. C* **2015**, *119* (8), 4126–4135.
- (97) Wang, D.; Wang, X.; Song, C. Comparative Study of Molecular Basket Sorbents Consisting of Polyallylamine and Polyethylenimine Functionalized SBA-15 for CO₂ Capture from Flue Gas. *ChemPhysChem* **2017**, *18* (22), 3163–3173.
- (98) Zhang, H.; Goeppert, A.; Olah, G. A.; Prakash, G. K. S. Remarkable Effect of Moisture on the CO₂ Adsorption of Nano-Silica Supported Linear and Branched Polyethylenimine. *J. CO₂ Util.* **2017**, *19*, 91–99.
- (99) Zhao, P.; Zhang, G.; Sun, Y.; Xu, Y. CO₂ Adsorption Behavior and Kinetics on Amine-Functionalized Composites Silica with Trimodal Nanoporous Structure. *Energy Fuels* **2017**, *31* (11), 12508–12520.
- (100) Leal, O.; Bolivar, C.; Ovalles, C.; García, J. J.; Espidel, Y. Reversible Adsorption of Carbon Dioxide on Amine Surface-Bonded Silica Gel. *Inorg. Chim. Acta* **1995**, *240* (1), 183–189.
- (101) Chang, A. C. C.; Chuang, S. S. C.; Gray, M.; Soong, Y. In-Situ Infrared Study of CO₂ Adsorption on SBA-15 Grafted with γ -(Aminopropyl)Triethoxysilane. *Energy Fuels* **2003**, *17* (2), 468–473.
- (102) Khatri, R. A.; Chuang, S. S. C.; Soong, Y.; Gray, M. Carbon Dioxide Capture by Diamine-Grafted SBA-15: A Combined Fourier Transform Infrared and Mass Spectrometry Study. *Ind. Eng. Chem. Res.* **2005**, *44* (10), 3702–3708.
- (103) Moore, J. K.; Sakwa-Novak, M. A.; Chaikittisilp, W.; Mehta, A. K.; Conradi, M. S.; Jones, C. W.; Hayes, S. E. Characterization of a Mixture of CO₂ Adsorption Products in Hyperbranched Aminosilica Adsorbents by ¹³C Solid-State NMR. *Environ. Sci. Technol.* **2015**, *49* (22), 13684–13691.
- (104) Lee, J. J.; Chen, C.-H.; Shimon, D.; Hayes, S. E.; Sievers, C.; Jones, C. W. Effect of Humidity on the CO₂ Adsorption of Tertiary Amine Grafted SBA-15. *J. Phys. Chem. C* **2017**, *121* (42), 23480–23487.
- (105) Yu, J.; Chuang, S. S. C. The Role of Water in CO₂ Capture by Amine. *Ind. Eng. Chem. Res.* **2017**, *56* (21), 6337–6347.
- (106) Chen, C.-H.; Shimon, D.; Lee, J. J.; Didas, S. A.; Mehta, A. K.; Sievers, C.; Jones, C. W.; Hayes, S. E. Spectroscopic Characterization of Adsorbed ¹³CO₂ on 3-Aminopropylsilyl-Modified SBA15 Mesoporous Silica. *Environ. Sci. Technol.* **2017**, *51* (11), 6553–6559.
- (107) Yu, J.; Zhai, Y.; Chuang, S. S. C. Water-Enhancement in CO₂ Capture by Amines: An Insight into CO₂-H₂O Interactions on Amine Films and Sorbents. *Ind. Eng. Chem. Res.* **2018**, *57* (11), 4052–4062.
- (108) Chen, C.-H.; Shimon, D.; Lee, J. J.; Mentink-Vigier, F.; Hung, I.; Sievers, C.; Jones, C. W.; Hayes, S. E. The “Missing” Bicarbonate in CO₂ Chemisorption Reactions on Solid Amine Sorbents. *J. Am. Chem. Soc.* **2018**, *140* (28), 8648–8651.
- (109) Bacsik, Z.; Ahlsten, N.; Ziadi, A.; Zhao, G.; Garcia-Bennett, A. E.; Martín-Matute, B.; Hedin, N. Mechanisms and Kinetics for

1522 Sorption of CO₂ on Bicontinuous Mesoporous Silica Modified with n-
 1523 Propylamine. *Langmuir* **2011**, 27 (17), 11118–11128.
 1524 (110) Danon, A.; Stair, P. C.; Weitz, E. FTIR Study of CO₂
 1525 Adsorption on Amine-Grafted SBA-15: Elucidation of Adsorbed
 1526 Species. *J. Phys. Chem. C* **2011**, 115 (23), 11540–11549.
 1527 (111) Aziz, B.; Hedin, N.; Bacsik, Z. Quantification of
 1528 Chemisorption and Physisorption of Carbon Dioxide on Porous
 1529 Silica Modified by Propylamines: Effect of Amine Density. *Micro-*
 1530 *porous Mesoporous Mater.* **2012**, 159, 42–49.
 1531 (112) Mafrá, L.; Čendak, T.; Schneider, S.; Wiper, P. V.; Pires, J.;
 1532 Gomes, J. R. B.; Pinto, M. L. Structure of Chemisorbed CO₂ Species
 1533 in Amine-Functionalized Mesoporous Silicas Studied by Solid-State
 1534 NMR and Computer Modeling. *J. Am. Chem. Soc.* **2017**, 139 (1),
 1535 389–408.
 1536 (113) Serna-Guerrero, R.; Da'na, E.; Sayari, A. New Insights into the
 1537 Interactions of CO₂ with Amine-Functionalized Silica. *Ind. Eng. Chem.*
 1538 *Res.* **2008**, 47 (23), 9406–9412.
 1539 (114) Yu, J.; Chuang, S. S. C. The Structure of Adsorbed Species on
 1540 Immobilized Amines in CO₂ Capture: An in Situ IR Study. *Energy*
 1541 *Fuels* **2016**, 30 (9), 7579–7587.
 1542 (115) Lee, J.-H.; Siegelman, R. L.; Maserati, L.; Rangel, T.; Helms,
 1543 B. A.; Long, J. R.; Neaton, J. B. Enhancement of CO₂ Binding and
 1544 Mechanical Properties upon Diamine Functionalization of
 1545 M₂(dobpdc) Metal–Organic Frameworks. *Chem. Sci.* **2018**, 9 (23),
 1546 5197–5206.
 1547 (116) Martell, J. D.; Porter-Zasada, L. B.; Forse, A. C.; Siegelman, R.
 1548 L.; Gonzalez, M. I.; Oktawiec, J.; Runčevski, T.; Xu, J.; Srebro-
 1549 Hooper, M.; Milner, P. J.; Colwell, K. A.; Autschbach, J.; Reimer, J.
 1550 A.; Long, J. R. Enantioselective Recognition of Ammonium
 1551 Carbamates in a Chiral Metal–Organic Framework. *J. Am. Chem.*
 1552 *Soc.* **2017**, 139 (44), 16000–16012.
 1553 (117) Bollini, P.; Choi, S.; Drese, J. H.; Jones, C. W. Oxidative
 1554 Degradation of Aminosilica Adsorbents Relevant to Postcombustion
 1555 CO₂ Capture. *Energy Fuels* **2011**, 25 (5), 2416–2425.